

# The Rise and Fall of ENSO in a Warming World: Insights from a Lag-Linear Model

P.J. Tuckman<sup>1\*</sup> and Da Yang<sup>1,2\*</sup>

<sup>1</sup>Department of Geophysical Sciences, University of Chicago, 5734 S  
Ellis Ave, Chicago, IL, 60637, United States of America.

<sup>2</sup>Department of Geophysics, Stanford University, 397 Panama Mall,  
Stanford, CA, 94305, United States of America.

\*Corresponding author(s). E-mail(s): [pjt5@uchicago.edu](mailto:pjt5@uchicago.edu);  
[dayang@stanford.edu](mailto:dayang@stanford.edu);

## Abstract

The El Niño-Southern Oscillation (ENSO) is a fluctuation in sea surface temperature (SST) and pressure across the equatorial Pacific Ocean with a period of 2-7 years. As the largest mode of interannual variability on Earth, ENSO shapes global weather and climate patterns ranging from monsoons in southern Asia to hurricanes in the Atlantic and droughts in South America. Predicting and understanding ENSO's response to greenhouse warming is essential for mitigating the impacts of climate change, yet model ensemble projections are prohibitively expensive to generate across emission scenarios and remain incompletely understood. Here, we use a hierarchy of models to show that ENSO strength undergoes a transient rise followed by a long-term fall under greenhouse warming. An East Pacific energy budget reveals that the initial increase in ENSO variability is due to enhanced upper-ocean stratification, while its subsequent decrease arises from a slowing Walker circulation and stronger surface flux damping. Building on these mechanisms, we derive a linear model which predicts the evolution of ENSO variability from only East Pacific temperature and stratification. We further show that subsurface warming, and therefore stratification, is connected to surface warming with a lag, enabling us to create a lag-linear model that explains ~90% of simulated changes in ENSO variability from only global mean SST and its history. This efficient predictor can forecast ENSO strength over time in any warming scenario, and reveals that faster emissions lead to stronger peak ENSO variability even with identical total emissions.

**Keywords:** ENSO, Climate Change, Greenhouse Warming

Every 2-7 years, the equatorial East Pacific becomes anomalously warm for several months in a phenomenon known as an “El Niño event” (Fig. 1a). These events disrupt society worldwide by lowering agricultural productivity [1], causing water shortages [2], and modulating weather and climate events such as floods [3], droughts, and tropical cyclones [4]. The last two extreme El Niño events, in 1997-1998 and 2015-2016, caused estimated economic productivity losses of up to \$4.1 and \$5.7 trillion, respectively, while their opposite, La Niña events, lead to much smaller economic gains [5]. Occurrences of El Niño and La Niña, along with corresponding changes in sea level pressure and the Walker circulation, are collectively known as the El Niño-Southern Oscillation (ENSO), and have been studied extensively over the last few decades [e.g., 6–8]. As the Earth warms during the 21st century, ENSO is expected to cause tens of trillions of dollars in economic losses [2, 5], yet the response of ENSO to different greenhouse gas emission scenarios remains expensive to predict and difficult to interpret [9, 10].

ENSO variability is measured as the standard deviation of equatorial East Pacific upper-ocean temperatures over time [11]. We represent changes in ENSO strength using:

$$\Delta M_{\text{ENSO}} = \frac{\text{East Pacific Temperature Standard Deviation}}{\text{Control East Pacific Temperature Standard Deviation}} - 1 \quad (1)$$

and smooth the result with a 20-year moving mean to remove unrelated internal variability. The “Control East Pacific Temperature Standard Deviation” represents ENSO variability in a control climate and is used so that  $\Delta M_{\text{ENSO}}$  is zero in that reference climate and positive when ENSO events are more extreme.

Climate model ensembles indicate that there will be a transient rise and permanent fall in ENSO variability under greenhouse warming. In observations, ENSO events strengthened during the final decades of the 20th century, likely in part due to anthropogenic emissions [Fig. 1c, dashed line, 12–14]. Most models predict that this enhanced ENSO variability will continue in the 21st century due to greenhouse warming increasing upper-ocean stratification [Fig. 1c, 13, 15], though model predictions of ENSO still have substantial spread [15–17]. This rise is temporary, however, and ENSO variability is expected to eventually decrease with warming [18], most clearly seen in simulations after an abrupt CO<sub>2</sub> increase (Fig. 1d). Similarly, idealized models under warming (Fig. 1b and e) display a transient peak of ENSO variability followed by a lasting decline, and simulations run past 2100 [19–21] or to equilibrium [22] show weaker ENSO events in warmer climates.

Here, we use idealized and comprehensive climate models and an East Pacific energy budget to derive a lag-linear model for ENSO strength in terms of global mean SST (equation in Fig. 1). The model accurately reproduces the rise and fall of ENSO variability, capturing between  $\sim 70\%$  and  $97\%$  of the signal across models and warming scenarios (Fig. 1 time series and panel f). We then use this simple model to gain insights into how greenhouse emissions control the future of ENSO events.

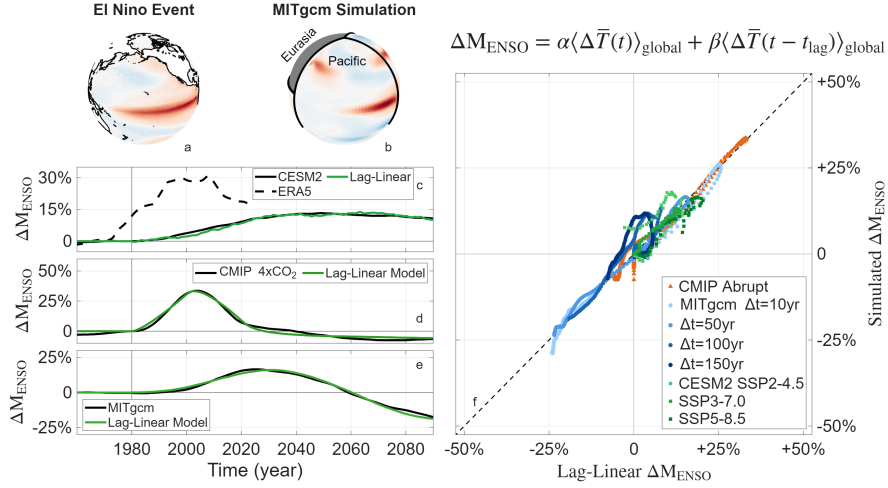


**Fig. 1** ENSO changes with warming and our lag-linear model for predicting these changes. The globes show an El Niño event from ERA5 (a) and the MITgcm idealized simulation (b). Panels c-e show  $\Delta M_{\text{ENSO}}$ , i.e., the normalized change in ENSO strength smoothed with a 20 year moving mean, and predictions based on the lag-linear model from ERA5 (c, dashed line), CESM2 under scenario SSP3-7.0 (c, solid line,  $R^2 = 0.97$ ), CMIP models under an abrupt quadrupling of  $\text{CO}_2$  (defined to occur in 1980, d,  $R^2 = 0.97$ ), and idealized MITgcm simulations (e,  $R^2 = 0.99$ ). The top right of the figure shows the equation for the lag-linear prediction, where  $\langle \bar{T} \rangle_{\text{global}}$  is the global mean SST and  $\alpha$ ,  $\beta$ , and  $t_{\text{lag}}$  are constant parameters. Panel f shows the relationship between the lag-linear prediction and the simulated changes in ENSO strength in all simulations studied (a CMIP ensemble, four MITgcm scenarios with differing warming timescales  $\Delta t$ , and three CESM2 scenarios). The combined  $R^2$  values across warming timescales are 0.67 for CESM2 and 0.93 for the MITgcm. The lag-linear parameters are allowed to vary across models, but are held constant across warming scenarios. The same quantities without the 20-year moving mean are shown in Extended Data Fig. 1.

## Fast El Niño and Slow La Niña Responses to Warming

We begin by showing that ENSO variability rises under warming due to differing changes in El Niño and La Niña events; greenhouse emissions cause an immediate rise in El Niño event temperatures, corresponding to ocean surface warming, while La Niña event temperatures, which are influenced by the subsurface, remain cool for several decades after warming begins (Fig. 2). To demonstrate this, we use a range of simulations and warming scenarios including: 1. an ensemble of CMIP models after an abrupt quadrupling of CO<sub>2</sub> [23] which exhibits fast warming over 30 years followed by slow warming over about a century (Fig. 2a.i dark green); 2. a Community Earth System Model Large Ensemble undergoing the SSP3-7.0 scenario [CESM2, 24] which exhibits an accelerating increase in mean East Pacific temperatures throughout the 21st century (Fig. 2a.i, light green); and 3. idealized atmosphere-ocean MITgcm simulations undergoing increasing longwave absorption over 10, 50, 100, or 150 years [continental configuration shown in the top-right of Fig. 2, temperature time series in Fig. 2a.ii, 25, 26].

In the abrupt warming simulations, 20-year maximum East Pacific temperatures (i.e., the temperature during strong El Niño events) rise immediately after the CO<sub>2</sub> increase, while 20-year minimum East Pacific temperatures (corresponding to strong La Niña events) remain nearly constant for two decades (Fig. 2a.i, dark red vs. dark blue line). Similarly, the CESM2 and MITgcm simulations show that minima temperature warming occurs two to three decades after maxima temperature warming (Fig. 2a).

Temperature maxima increase before temperature minima because ENSO alters equatorial East Pacific upwelling. Temperatures during El Niño events, when upwelling is suppressed and zonal asymmetries across the tropical Pacific are small, warm at the same rate as tropical mean near-surface water (Fig. 2b, red lines). La Niña events, on the other hand, enhance upwelling, so their rise in temperature is slowed by cooler subsurface water entering the mixed layer (Fig. 2b, blue lines). In other words, as atmospheric temperatures increase, the near-surface ocean warms before the subsurface, leading to increased El Niño temperatures and temporarily enhanced ENSO variability. The importance of contrasting near- and subsurface behavior suggests that the rise in ENSO strength shown in Fig. 1 depends strongly on stratification [consistent with previous work: 13, 15]; we now study this quantitatively with an equatorial East Pacific energy budget.

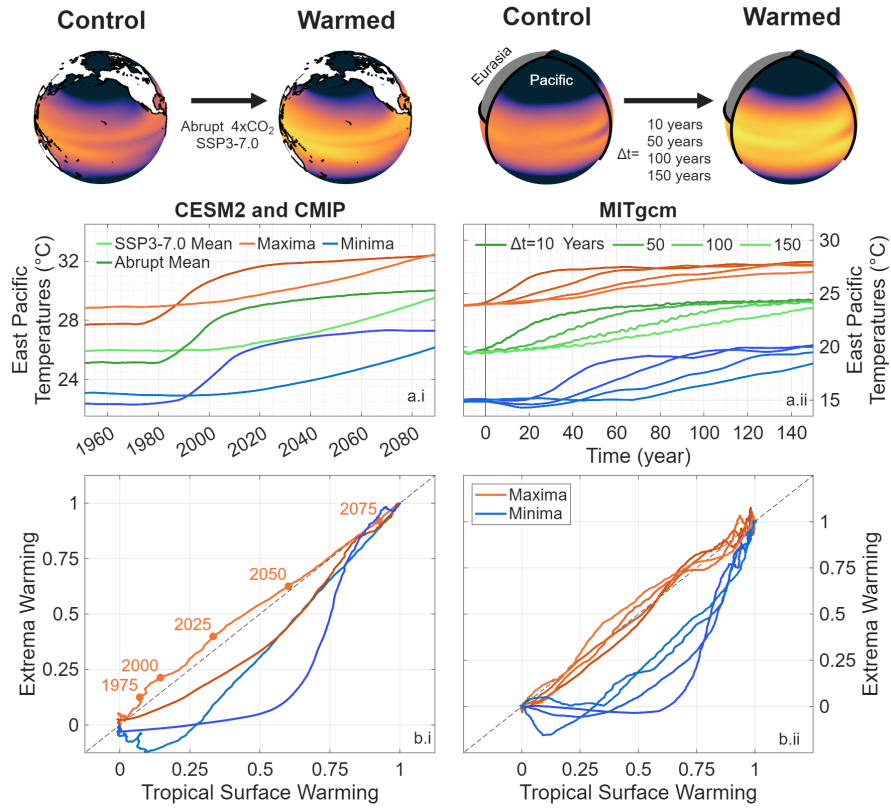


**Fig. 2** The simulations used in this study and how relevant quantities change with warming. The top row shows the change in climatological (20-year moving mean) SSTs under warming in the full climate model simulations (left) and the idealized MITgcm simulations (right), as well as indicating the warming scenarios. Panel a shows changes in East Pacific moving mean, minima, and maxima temperatures over time for each simulation, and panel b shows how the moving minima and maxima warming relate to changes in the moving mean temperature of the tropical ocean surface.

## Energy Balance of the Equatorial East Pacific

We use an energy budget of the equatorial East Pacific to reproduce simulated changes of ENSO variability in the MITgcm, showing that ENSO's transient rise is associated with enhanced upper-ocean stratification and that its long-term fall is associated with decreasing stratification, a weakening mean Walker circulation, and strengthening surface flux damping (Fig. 3). The anomalous temperature of the mixed layer is given by:

$$\frac{d}{dt}\langle T' \rangle = -\langle \bar{\mathbf{u}} \cdot \nabla T' \rangle - \langle \mathbf{u}'_h \cdot \nabla_h \bar{T} \rangle - \langle w' \bar{\Gamma} \rangle - \bar{\alpha}_{\text{SF}} \langle T' \rangle_{2\text{D},\text{surf}} \quad (2)$$

where  $\langle \cdot \rangle$  indicates a volume average over the equatorial East Pacific ( $\sim 205 - 263^\circ\text{E}$ , within  $\sim 5$  degrees of the equator, top 80 m),  $T$  is temperature,  $\mathbf{u}$  is the three-dimensional (3D) current,  $\nabla$  is the 3D gradient, the  $h$  subscript represents horizontal quantities,  $w$  represents the vertical current,  $\Gamma$  is the stratification ( $dT/dz$ ), bar variables (e.g.,  $\bar{T}$ ) represent the average climate through 20-year moving means, and prime variables (e.g.,  $T'$ ) represent ENSO anomalies as deviations from this temporal mean with the seasonal cycle removed. The association of  $\langle T' \rangle$  with ENSO is supported by a spectral analysis showing that most anomalous East Pacific temperature variability occurs in the 2-7 year ENSO band. The final term of Eq. 2 treats anomalous surface fluxes and longwave radiation (i.e., thermodynamic damping) as the product of a slowly varying coefficient  $\bar{\alpha}_{\text{SF}}$  and the anomalous regional SST. We omit the small non-linear terms and advection associated with the seasonal cycle for clarity; they are included in the calculations (details in the methods section). Additionally, we treat the mixed layer as a fixed volume, though the mean thermocline depth may change over time.

We turn Eq. 2 into an expression for the magnitude of ENSO peaks in a given climate by dividing both sides by  $\langle T' \rangle$ , integrating from the initiation of an El Niño event to its peak, and normalizing by a reference budget (details in methods section):

$$\Delta M_{\text{ENSO}}(t) = \exp \left[ \int_{\tau_0}^0 \Delta \sigma d\tau \right] - 1, \quad (3)$$

where

$$\Delta \sigma \equiv -\frac{\langle \Delta \bar{\mathbf{u}} \cdot \nabla T' \rangle}{\langle T' \rangle} - \frac{\langle \mathbf{u}'_h \cdot \Delta \nabla_h \bar{T} \rangle}{\langle T' \rangle} - \frac{\langle w' \Delta \bar{\Gamma} \rangle}{\langle T' \rangle} - \Delta \bar{\alpha}_{\text{SF}} \frac{\langle T' \rangle_{2\text{D},\text{surf}}}{\langle T' \rangle}. \quad (4)$$

Changes in the ENSO growth rate,  $\Delta \sigma$ , represent how unstable the tropical Pacific is to El Niño perturbations [similar to the commonly used Bjerknes index, 27, discussed below]. In these expressions,  $\Delta$  represents a change from the reference value,  $\tau_0$  marks the initiation of an ENSO event defined by a fixed small value of  $\langle T' \rangle$ , and  $\tau = 0$  marks the event's peak. By setting this expression equal to  $\Delta M_{\text{ENSO}}$ , we assume that  $\langle T' \rangle$  peak values are proportional to East Pacific standard deviation; this is supported by simulation results (Extended Data Fig. 2). To evaluate changes in ENSO growth rate, the climatological variables in Eq. 3 (e.g.,  $\bar{\Gamma}$ ) are allowed to vary with warming while

the structure of an El Niño event (represented by, e.g.,  $w'(\mathbf{x}, \tau)/\langle T' \rangle$  and  $\tau_0$ ) is held fixed [as in the Bjerknes index, 27]. This allows us to understand how mean climate variables alter ENSO strength by placing the same El Niño event in a changing climate (details of this calculation and demonstration of constant ENSO structure are shown in methods section).

Under climate change, upper-ocean currents weaken while stratification first increases then decreases. In the reference climate (Fig. 3a.i) water moves west near the surface, leading to upwelling and cooler water in the East Pacific. Once greenhouse warming begins (a.ii), surface temperatures increase significantly (by  $\sim 4\text{K}$ ) while the subsurface has not yet experienced much warming ( $\sim 1\text{-}2\text{ K}$ ), enhancing stratification. Over time, the subsurface ocean warms as well, and the stratification settles to an equilibrium value (a.iii). In this warmer climate, mean currents have decreased (especially near the surface), associated with a slower Walker circulation leading to weaker trade winds [Fig. S1; 22, 28–30].

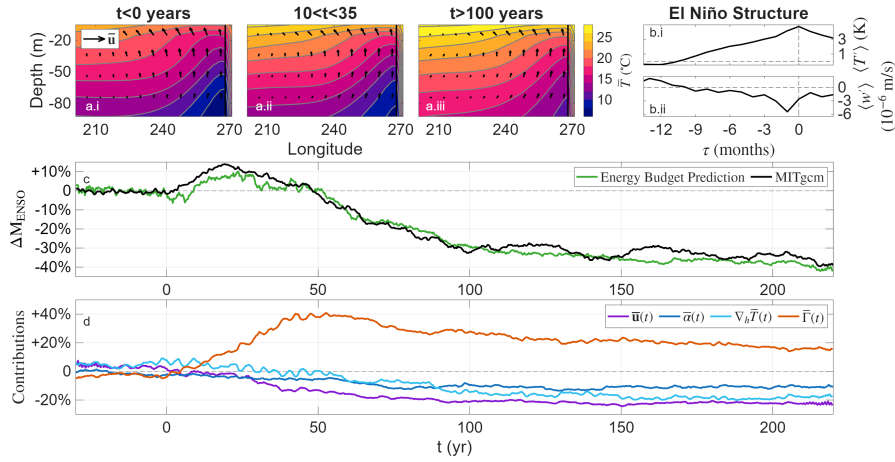


**Fig. 3** Using energy balance to study how the magnitude of El Niño events changes under warming in the MITgcm  $\Delta t = 50$  years simulations. Panel a shows the mean temperature (color) and currents (arrows) in the pre-warming climate (a.i), the transient warming state (a.ii), and the (mostly) equilibrated warmed state (a.iii). Panel b shows the volume averaged anomalous temperature (b.i) and vertical velocity (b.ii) from a composite El Niño structure in the reference climate. Panel c shows the predicted  $\Delta M_{\text{ENSO}}$  from energy balance and compares it to the simulated results. Panel d shows how specific terms affect the predicted ENSO magnitude.

The structure of ENSO events, meanwhile, is calculated as a composite across 25 El Niño events in the reference climate, identified as the largest maxima of  $\langle T' \rangle$  separated by at least two years. In this composite, volume averaged anomalous temperature ( $\langle T' \rangle$ , panel b.i) grows from zero to about 4 K over the  $\sim 10$  months before a peak, and the anomalous vertical velocity ( $\langle w' \rangle$ , b.ii) becomes strongly negative.

Combining the evolution of mean variables and a fixed ENSO structure, our energy budget predicts a transient rise and long-term fall in ENSO strength (Fig. 3c), matching the simulations in showing that  $\Delta M_{\text{ENSO}}$  increases to about +10% from year 0 to year 20, then slowly decreases to about -40%.

Eq. 3 is similar to the Bjerknes index [27, 31] in that it uses an anomalous energy budget to predict ENSO variability by assuming a fixed El Niño structure while allowing mean variables to evolve as the climate changes. This method is different from the Bjerknes index in that 1. the quantities are volume averaged after multiplication (i.e., we use  $\langle u' \nabla_x \bar{T} \rangle$  rather than  $\langle u' \rangle \langle \nabla_x \bar{T} \rangle$ ), 2. it does not assume anything about the meridional structure of ENSO temperature anomalies, and 3. we allow El Niño structure (e.g.,  $\mathbf{u}' / \langle T' \rangle$ ) to vary over space and time ( $\tau$ ). This leads to a more accurate but complex predictor of ENSO strength in an evolving climate.

Using Eq. 3, we can attribute the evolution of El Niño strength to individual variables by changing only that variable over time. The Walker circulation weakens with warming [Fig. S1; 22, 28–30], leading to the mean velocity term ( $\bar{\mathbf{u}}$ , commonly known as dynamical damping) and the mean horizontal temperature gradient term ( $\nabla_h \bar{T}$ ) contributing less to ENSO growth (Fig. 3d). The surface flux term ( $\bar{\alpha}_{\text{SF}}$ , thermodynamic damping) also causes a weakening of ENSO variability over time due to the exponential relationship between saturation humidity and temperature. As the saturation specific humidity of a parcel of air increases exponentially with warming, the same relative humidity corresponds to a larger saturation deficit, and therefore stronger evaporation, in a warmer climate (see Supplementary Text 1 and Extended Data Fig. 3 for details).

The transient strengthening of ENSO events, meanwhile, is associated with changes in stratification (known as the vertical advective or Ekman feedback). As the surface of the ocean responds immediately to greenhouse warming while the response of the subsurface ocean is delayed (Fig. 2b.ii and Fig. 3a), upper-ocean stratification first increases over 50 years then decreases over the following centuries. These stratification changes contribute to a fast increase then slow decrease of ENSO variability, which, combined with other mean climate changes, cause a transient rise and permanent fall in ENSO strength.

## Simple Predictors of ENSO Variability

We now use the East Pacific energy budget to derive a linear model for ENSO variability in terms of mean temperature and stratification (Fig. 4). As the argument to the exponential in Eq. 3 is small, we can apply a Taylor expansion to create a linear expression for  $\Delta M_{\text{ENSO}}$  (see Supplementary Text 2 for details). Then, by multiplying the stratification term by  $\langle \Delta \bar{\Gamma} \rangle / \langle \Delta \bar{\Gamma} \rangle$  and each other term by  $\langle \Delta \bar{T} \rangle / \langle \Delta \bar{T} \rangle$ , we find:

$$\Delta M_{\text{ENSO}}(t) = A \langle \Delta \bar{T} \rangle + B \langle \Delta \bar{\Gamma} \rangle, \quad (5)$$

where

$$A = -\frac{1}{\langle \Delta \bar{T} \rangle} \int_{\tau_0}^0 d\tau \left( \frac{\langle \Delta \bar{\mathbf{u}} \cdot \nabla T' \rangle}{\langle T' \rangle} + \frac{\langle \mathbf{u}'_h \cdot \Delta \nabla_h \bar{T} \rangle}{\langle T' \rangle} + \Delta \bar{\alpha}_{\text{SF}} \frac{\langle T' \rangle_{2\text{D}, \text{surf}}}{\langle T' \rangle} \right) \text{ and} \quad (6a)$$

$$B = -\frac{1}{\langle \Delta \bar{\Gamma} \rangle} \int_{\tau_0}^0 d\tau \frac{\langle w' \Delta \bar{\Gamma} \rangle}{\langle T' \rangle}. \quad (6b)$$

The parameters  $A$  and  $B$  are roughly constant in the MITgcm simulations:  $A\langle\Delta\bar{T}\rangle$  and  $B\langle\Delta\bar{\Gamma}\rangle$  have strong linear relationships with  $\langle\Delta\bar{T}\rangle$  and  $\langle\Delta\bar{\Gamma}\rangle$ , respectively (demonstrated in the  $\Delta t = 50$  year scenario, Fig. 4a and b). Intuitively, the value of  $1/A$  ( $\sim 7$  K) is an e-folding scale for ENSO strength (Eq. 3), while  $1/B$  is analogous but for stratification. These constants are made up of changes to components of the growth rate ( $\Delta\sigma$ , Eq. 4) and each therefore corresponds to components of the Bjerknes index (i.e.,  $A$  is made up of dynamical damping, zonal advective feedback, the thermocline feedback, and thermodynamic damping, while  $B$  is controlled by the Ekman feedback). Overall, Eq. 5 is an energy balance based linear predictor for ENSO strength in terms of only mean temperature and mean stratification.

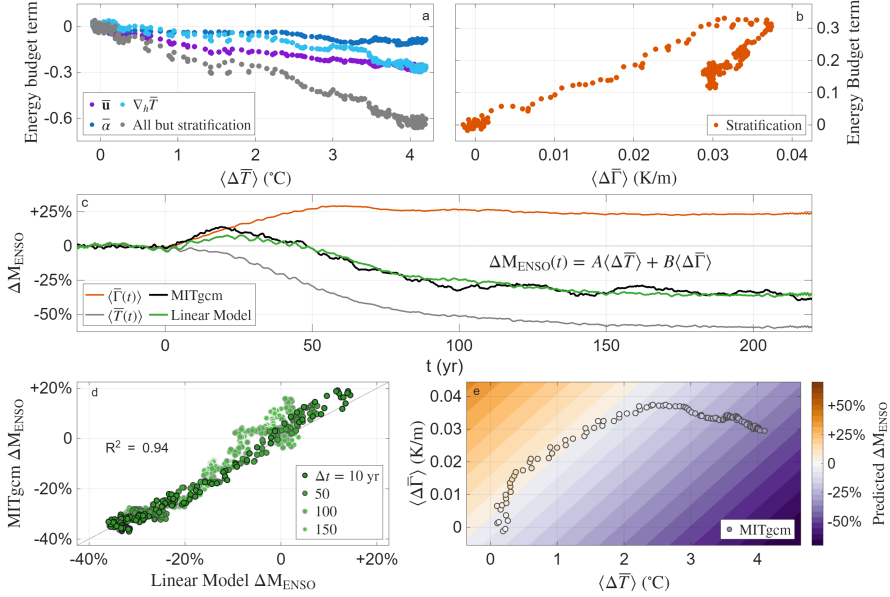


**Fig. 4** Our first linear model for ENSO variability. Panel a shows the relationship between three of the energy budget terms and mean temperature in the MITgcm  $\Delta t = 50$  year simulations, while panel b shows the relationship between the stratification term and mean stratification. Panel c shows the simulated ENSO strength from the MITgcm, the empirically fit linear model and its prediction as a function of time, as well as the predictions if only mean temperature or stratification were allowed to change. Panel d compares the simulated ENSO magnitude to that predicted by the linear model for all MITgcm simulations, where color corresponds to mean temperature and point outlines correspond to different warming rates. Panel e illustrates how this linear model predicts ENSO magnitude would change as a function of the two controlling variables, with the  $\Delta t = 50$  year simulation data shown as a scatterplot.

The linear model accurately predicts the evolution of simulated ENSO variability (Fig. 4c). We can estimate  $A$  and  $B$  either by evaluating expressions 6a and 6b (calculated as the slope of the data in Fig. 4a and b) or through an empirical fit of  $\Delta M_{\text{ENSO}}$ ; these two methods give similar results (Extended Data Table 1). The simplicity of the model allows for easy separation of the effects of mean temperature and stratification: warming causes a monotonic weakening of ENSO variability, while stratification

changes cause a fast increase then a small decrease in ENSO strength (Fig. 4c). It is important to note that the contributions of stratification changes to ENSO variability are not fully captured by a linear function of mean stratification (non-linearity in Fig. 4b), so its role in the long-term weakening of ENSO is smaller in the linear model than in the energy balance framework.

Eq. 5 can also predict ENSO variability in simulations under different warming scenarios with  $A$  and  $B$  coefficients determined from only the  $\Delta t = 50$  year simulations (Fig. 4d). In other words, as the climate warms, just two variables, mean temperature and stratification, are enough to predict the strength of ENSO variability regardless of the emissions scenario (Fig. 4e). This allows for the prediction of ENSO strength across warming scenarios, even if the MITgcm is run for only one realization, simply by tracing the path of the two relevant variables.

### Predicting ENSO from Surface Temperature Evolution

Building on Eq. 5, we develop a lag-linear model for ENSO variability in terms of global mean SST by connecting stratification changes to subsurface warming and thereby SST changes with a lag (Fig. 5). In the control climate, easterly trade winds and the Coriolis effect cause near-surface poleward currents throughout the tropics. The mass moving away from the equator is replaced by strong upwelling, and water returns from the subtropics to the equator at depth [Fig. 5a, 32, 33]. This circulation, or the ocean’s “subtropical cells,” controls the timescale over which subsurface water on the equator responds to greenhouse warming.

By diagnosing a simulation’s subtropical cells, we can calculate an expected replacement time of equatorial subsurface water. The MITgcm simulations have downwelling from  $\sim 15^\circ\text{N}$  to  $\sim 30^\circ\text{N}$  and the sinking water moves equatorward beneath the surface. Dividing the position of downwelling (estimated at  $\phi_\downarrow \approx 21^\circ$ ) by a representative southward velocity ( $v_{\text{stc}} \approx 1.9$  mm/s, calculated as the harmonic mean with respect to latitude) gives an expected subtropical cell timescale, or how long it takes for surface water to replace equatorial subsurface water ( $t_{\text{stc}} = \phi_\downarrow/v_{\text{stc}} = 41$  years). Note that we assume the two hemispheres have similar subtropical cells; this is likely as we are studying an ocean region with no hemispherically asymmetric continents and the trade winds are centered near the equator.

The timescale of the subtropical cells matches the lag between rising El Niño and La Niña temperatures (Fig. 5b). As discussed previously, temperature maxima increase at almost exactly the same rate as regional surface temperatures, while temperature minima, as well as subsurface water, warm several decades later. This observed lag matches the diagnosed  $t_{\text{STC}}$  based on the simulations’ currents and, crucially, indicates that the delayed response of warming at depth does not depend on the warming timescale.

It is now possible to predict ENSO strength from surface temperature and its history using the connection between temperature at depth and subtropical surface temperatures with a lag. We assume that surface warming in each region (i.e., the equatorial East Pacific and the subtropical Pacific) is proportional to global mean SST increases and that East Pacific mixed layer temperatures are proportional to East Pacific surface temperatures (Fig. S2a), leading to a lag-linear model of the form:

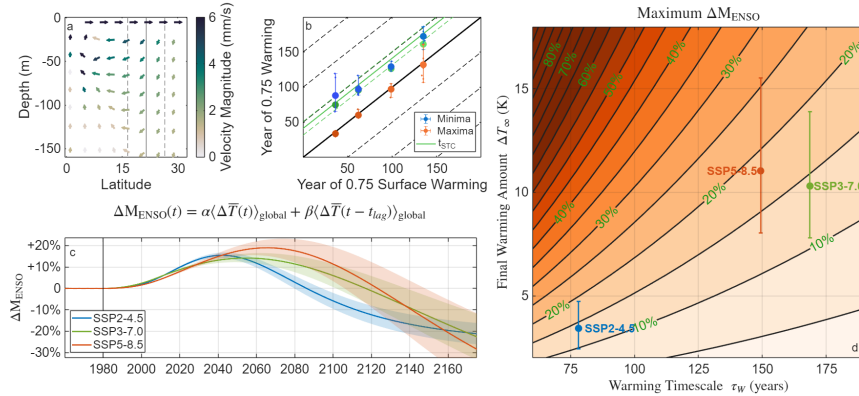


**Fig. 5** Developing a lag-linear model for ENSO variability in terms of global mean surface temperature. (a) Currents as a function of latitude and depth, with the characteristic latitude of descent (solid) and rough uncertainty range (dashed) indicated with vertical lines. (b) The year after warming begins that temperature maxima (red) and temperature minima (blue) reach three quarters of their final warming, and the same for temperature at depth (green) as a function of mean surface tropical temperature warming timescale. The solid black line represents no delay between surface warming and the quantity in question (i.e.,  $x=y$ ), the dashed black lines represent delays in intervals of 50 years, the solid green line represents a delay of  $t_{STC} = 41$  years, and the dashed green lines represent an uncertainty around this value (calculated from the range of downwelling latitudes). Below panels a and b is the lag-linear model equation. (c) ENSO magnitude changes predicted from the lag-linear model in various warming scenarios, the temperature trajectories are shown in Extended Data Fig. 5. (d) How peak ENSO magnitude predicted by the lag-linear model depends on the total amount of warming ( $\Delta T_{\infty}$ ) and the warming timescale ( $\tau_W$ ), with the common SSP scenarios marked.

$$\Delta M_{ENSO}(t) = \alpha \langle \Delta \bar{T}(t) \rangle_{\text{global}} + \beta \langle \Delta \bar{T}(t - t_{\text{lag}}) \rangle_{\text{global}} \quad (7)$$

where  $\langle \bar{T} \rangle_{\text{global}}$  is the global mean SST,  $t_{\text{lag}}$  is a timescale which represents how long it takes for warming to reach the subsurface in the East Pacific, and  $\alpha$  and  $\beta$  are constants (empirically fit values in Extended Data Table 2, quantitatively related to  $A$  and  $B$  in Supplementary Text 3).

The lag-linear model, using the same values of  $\alpha$ ,  $\beta$ , and  $t_{\text{lag}}$ , accurately predicts ENSO variability across MITgcm warming scenarios (Fig. 1e and f,  $R^2 = 0.93$ ). Additionally, the vital time lag parameter is possible to diagnose from the ocean circulation; the fit  $t_{\text{lag}}$  in the MITgcm is about 35 years, close to  $t_{\text{stc}} = 41$  years. Similarly, the lag-linear model (with different parameters) works in CESM2 (Fig. 1c,  $R^2 = 0.97$  for SSP 3-7.0,  $R^2 = 0.67$  across all scenarios using parameters fit to the SSP 3-7.0 data) and CMIP ensemble simulations (Fig. 1d,  $R^2 = 0.97$ ). The subtropical timescale can also be diagnosed from the CESM2 simulations as  $t_{\text{stc}} = 24$  years, close to the fit value of  $t_{\text{lag}} = 28$  years.

The values of  $\alpha$  and  $\beta$  vary considerably across models (Extended Data Table 2) due to 1. differing simulated ENSO responses to warming (Extended Data Fig. 4) and 2. differing relationships between global mean warming and regional East Pacific warming (Fig. S2b). As GCMs predict different responses of ENSO to the same emissions scenario [5, 15, and Extended Data Fig. 4], our linear predictors must use different parameters to approximate each model. The  $\alpha$  and  $\beta$  values fit to the MITgcm and

CESM2 are both within the CMIP model spread for those parameters (diagnosed from ENSO peak and steady-state amplitudes), indicating that physical model differences in simulating ENSO, rather than biases in the linear model derivation, lead to variations in  $\alpha$  and  $\beta$ . The values of  $\alpha$  and  $\beta$  also differ between GCMs because the proportionality constant between East Pacific surface temperature and global mean surface temperature is different in CESM2, the CMIP ensemble, and the MITgcm (by up to a factor of 3, Fig. S2b). Despite quantitative inter-model disagreement in the parameters, the accuracy of the lag-linear predictor is robust across all studied cases.

The simplicity of the lag-linear model allows us to quickly predict ENSO variability from any surface temperature trajectory. To demonstrate this, we fit data from commonly used CESM2 emission scenarios to global mean SST trajectories of the form:

$$\langle \Delta \bar{T} \rangle_{\text{global}} = \Delta T_{\infty} \frac{(t/\tau_W)^{\kappa}}{1 + (t/\tau_W)^{\kappa}} \quad (8)$$

where the three parameters are 1.  $\Delta T_{\infty}$  representing the warming amplitude, 2.  $\tau_W$  representing a warming timescale, and 3.  $\kappa$  representing the abruptness of warming when greenhouse emissions begin (time series in Extended Data Fig. 5).

Using these simulated temperature trajectories, the lag-linear model can estimate ENSO variability from few model realizations (Fig. 5c). As would be expected, ENSO variability in each scenario first rises and then falls to well below the preindustrial value. In the SSP2-4.5 scenario (“Middle of the Road”), ENSO variability reaches up to 15% higher than preindustrial levels and remains elevated through about 2075. Interestingly, ENSO variability peaks slightly lower in the SSP3-7.0 scenario (“Regional Rivalry”), but remains elevated for significantly longer, until about 2100. In the SSP5-8.5 scenario (“Fossil-fueled Development”), ENSO variability reaches about 20% higher than preindustrial levels and remains elevated into the 22nd century.

More generally, Eq. 7 and 8 together can predict how peak ENSO variability depends on warming timescale and amplitude (Fig. 5d). Unsurprisingly, stronger warming scenarios (i.e., larger  $\Delta T_{\infty}$ ) at a constant warming timescale lead to larger peak amplitudes. In fact,  $\Delta M_{\text{ENSO}}$  is proportional to  $\Delta T_{\infty}$  at all times (clear from substituting Eq. 8 into Eq. 7). Much more interestingly, peak ENSO amplitude also depends strongly on the warming timescale  $\tau_W$ ; shorter timescales (faster emissions) lead to larger ENSO peaks even if the total emissions are the same. This explains the predictions from SSP2-4.5 and SSP3-7.0 in panel c; while SSP3-7.0 has significantly more warming ( $\Delta T_{\infty} \sim 10$  K vs. 3.5 K), the warming occurs over much longer ( $\tau_W \sim 170$  years vs. 80), so the peak ENSO amplitude is similar. Intuitively, if subsurface warming can keep pace with surface warming, then peak ENSO amplitude is limited, while if significant warming occurs suddenly, ENSO variability increases drastically.

## Discussion

El Niño and La Niña events control a large part of climate’s impact on society by altering large-scale circulations and global weather patterns. Under greenhouse warming, ENSO variability exhibits a transient rise and then a permanent fall, resulting in

weaker ENSO events in an equilibrated warmer climate. Here, we have shown that the differing short and long-term responses of ENSO to warming are connected to stratification and mean climate changes: enhanced ENSO strength comes from an immediate increase in surface temperatures, while the subsequent reduced ENSO strength is associated with 1. a warming subsurface and 2. a slower Walker circulation and stronger surface flux damping. We use this understanding to develop two simple linear models, one based on East Pacific temperature and stratification, and one based on global mean surface temperature and its history, both of which can predict ENSO variability quickly and accurately. These simple linear models demonstrate that the timescale of warming is vital in controlling the response of ENSO to greenhouse emissions; fast warming will lead to very strong ENSO events before their eventual weakening, while slower warming moderates this peak and prevents the most extreme impacts. This implies that a given amount of greenhouse gas emissions can have different effects at different times, i.e., that the social cost of carbon is strongly time-dependent.

The differing response timescales of the surface and subsurface ocean, and therefore the differing short and long-term effects of greenhouse warming, have significant implications for the study of the equatorial East Pacific in a changing climate. The climatological East Pacific temperature is influenced by upwelling just as much as ENSO, so delayed subsurface warming is critical for understanding the region’s response to climate change [34]. Future research focused on biases in the subtropical cell timescale may reveal why the East Pacific experiences too much short-term warming in simulations [35, 36] and help us understand the well-known “pattern effect” [37, 38].

With respect to broader climate research, the utility of our linear models indicates that simple predictors could be used to study a wide range of phenomena across different regimes. For example, ENSO in paleoclimate contexts may depend on relatively few variables such as basin width and mean temperature, and might therefore be explainable with simple models. Similarly, other climate modes (such as the North Atlantic Oscillation or Pacific Decadal Oscillation) may change under greenhouse warming mostly in proportion to mean temperature and one or two other variables, giving the techniques used here broad applicability.

Finally, our quick and accurate lag-linear model allows for the prediction of ENSO impacts in a wide range of scenarios across which it would be computationally impossible to run a CMIP ensemble. To reliably diagnose ENSO strength over time from Earth system models requires perhaps a dozen realizations from each of several models, and so is often prohibitively expensive. Forecasts of phenomena affected by ENSO need to consider how El Niño events will evolve over time; using our lag-linear model as a proxy for future ENSO variability can accelerate research on topics ranging from monsoon variability to tropical cyclones. Overall, the societal impact of climate change will depend strongly on the evolution of ENSO variability, so a fast prediction method for this crucial quantity will allow for a more accurate calculation of the social cost of carbon across emission scenarios and help society better prepare for future climate extremes.

## Methods

We now give details on the methods used in this work, beginning with a description of the comprehensive and idealized climate models, followed by a discussion of ocean energy balance and how it is used to predict ENSO variability over time.

### Comprehensive Models

Our most accurate predictions of future ENSO variability come from models participating in the Sixth Climate Model Intercomparison Project [CMIP6, 23]. We use CESM2 to understand how ENSO responds to commonly used SSP emission scenarios; all quantities displayed for the SSP3-7.0 scenario (Fig. 1) are the mean across 100 realizations from the CESM2 Large Ensemble Community Project [39], while all quantities for the SSP2-4.5 and SSP5-8.5 scenarios (Fig. 1f and Fig. 5) are the average across 15 realizations. For each SSP, time series from the historical run and that emissions scenario are concatenated before averaging across realizations. Additionally, when fitting temperature curves to each warming scenario (Extended Data Fig. 5), we employ temperature predictions at 2300 from Lee et al. [40, using the MAGICC7 emulator]. These long-term predictions are included in the fitting process and their uncertainties are taken to be the uncertainty in  $\Delta T_\infty$ .

To study how ENSO responds to abrupt greenhouse warming, we use an ensemble of the following models, chosen because they have sufficient data in preindustrial control simulations (piControl) and abrupt quadrupling of CO<sub>2</sub> simulations (abrupt4xCO<sub>2</sub>):

- ACCESS-CM2
- AWI-CM-1-1-MR
- BCC-CSM2-MR
- BCC-ESM1
- CESM2-FV2
- CESM-WACCM-FV2
- CESM2-WACCM
- CESM
- CMCC-CM2-SR5
- CNRM-CM6-1
- CanESM5
- E3SM-1-0
- FGOALS-g3
- GFDL-ESM4
- GISS-E2-1-G
- INM-CM4-8
- INM-CM5-0
- IPSL-CM6A-LR
- MPI-ESM-1-2-HAM
- MPI-ESM1-2-LR
- MRI-ESM2-0
- NorCPM1
- NorESM2-MM
- TaiESM1
- UKESM1-0-LL

For each realization (one for most models listed, two from CanESM5 and three from GISS-E2-1-G), the last 50 years from piControl runs are concatenated with the first 150 years from abrupt4xCO<sub>2</sub> runs.

For all CESM2 and CMIP data, surface temperatures (variable name `ts`, defined as the temperature at the lower boundary of the atmosphere) averaged from 225-260° longitude within 5 degrees of the equator represent the East Pacific while data averaged from 160-260° longitude within 10 degrees of the equator represents the tropical Pacific (Fig. 2b).

## MITgcm Simulations

To study ENSO in an idealized setting, we run simplified MITgcm simulations [25] in configurations based on those in Tuckman et al. [26, 41]; the code for the control run is available at [https://github.com/MITgcm/verification\\_other/tree/master/cpl\\_gray%2Bswamp%2Bocn](https://github.com/MITgcm/verification_other/tree/master/cpl_gray%2Bswamp%2Bocn). The model has a West Pacific warm pool and East Pacific cold tongue comparable to those in observations, as well as tropical easterlies, extratropical westerlies, and an ENSO mode with approximately correct spatial and temporal patterns [26, 41].

The MITgcm simulations use cubed-sphere grids with  $\sim 2.8^\circ$  resolution in the tropics for the atmosphere and ocean [42], have 26 vertical levels in the atmosphere, and have 43 vertical levels in the ocean (with more levels near the surface). The atmosphere has idealized moist physics and a gray radiation scheme [43] which includes water vapor feedback on long-wave optical thickness [44] but does not include clouds or shortwave absorption by the atmosphere. There is a seasonal cycle of incident shortwave radiation appropriate for a circular orbit with an obliquity of  $23.45^\circ$ . The ocean has a uniform depth of 3.4 km and uses the mixing scheme developed in Gaspar et al. [45].

The model’s continental configuration consists of a large landmass meant to represent Eurasia which extends from  $0$ - $135^\circ\text{E}$  and from  $\sim 8^\circ\text{N}$  to the North Pole. This landmass is treated as a 2m slab ocean so that it has a low heat capacity and no ocean dynamics. Other continents are represented as thin barriers that block ocean flow: two barriers at  $0$  and  $270^\circ\text{E}$  extend from  $35^\circ\text{S}$  to the North Pole to isolate the Atlantic basin, and one extends from  $30^\circ\text{S}$  to the southeast corner of the continent to separate the Indian and Pacific basins.

The MITgcm is run for 750 years in a control, preindustrial-like climate, then a time-stepping parameter (`abEps` in the code) is branched to slightly different values so as to create different realizations without changing the physics of the model. Thirty years after the time-stepping parameter is modified, at a time defined to be  $t = 0$  years, greenhouse warming begins through an increase in the longwave absorption efficiency of  $\text{CO}_2$  ( `$\tau_{\text{CO}_2}$`  or `ir_tau_co_2` in the code). Over the following  $\Delta t$  (10, 50, 100, or 150 years),  $\tau_{\text{CO}_2}$  increases linearly from 0.8678 to 1.3017. In addition to one control run in which  $\tau_{\text{CO}_2}$  is not changed, there are 5, 9, 4, and 9 realizations used for the four values of  $\Delta t$ .

## ENSO Magnitude Prediction from Energy Balance

Here, we explain in detail the energy balance framework used to study how and why the magnitude of ENSO events changes as the climate warms. This method is similar to the Bjerknes index [27] which predicts how ENSO variability changes from mean variables. Unlike the Bjerknes index, our method 1. evaluates products before taking volume averages, 2. includes anomalous meridional advection, 3. makes no assumptions about the meridional structure of temperature anomalies, and 4. allows relationships between anomalous variables to depend on  $\tau$ . Both methods assume a constant structure of ENSO as the climate warms and treat surface fluxes as a linear damping term. We begin with a general ocean energy budget then apply it to predicting ENSO variability.

Temperature tendency in the ocean is given by:

$$\frac{\partial}{\partial t}T(\mathbf{x}, t) = -\nabla \cdot (\mathbf{u}T) + \frac{\partial}{\partial z}F_{\text{SGS}}$$

where  $T$  is temperature as a function of space ( $\mathbf{x}$ ) and time ( $t$ ),  $\mathbf{u}$  is the 3d-current,  $\nabla \cdot$  is the 3d divergence, and  $F_{\text{SGS}}$  represents any sub-grid-scale or diabatic process including mixing, radiation, and turbulent fluxes (i.e., sensible heat and evaporation). It is assumed that the sub-grid-scale forcing acts only vertically.

As we wish to study anomalous temperatures, each variable (e.g.,  $T$ ) is separated into a 20-year moving mean ( $\bar{T}$ ), a mean seasonal cycle ( $\tilde{T}$ ), and an anomaly ( $T' = T - \bar{T} - \tilde{T}$ ). The anomalous temperature budget is:

$$\frac{\partial}{\partial t}T'(\mathbf{x}, t) = -(\nabla \cdot \mathbf{u}T')' + \frac{\partial}{\partial z}F'_{\text{SGS}}.$$

We now decompose the flux-form advection term into an advective-form term and a flux-form correction  $\text{FF}'_{\text{corr}}$  defined such that  $(\nabla \cdot \mathbf{u}T')' = (\mathbf{u} \cdot \nabla T')' + \text{FF}'_{\text{corr}}$ . As seawater is effectively incompressible,  $\text{FF}'_{\text{corr}}$  should be zero, but because data for  $\mathbf{u}$  and  $T$  are evaluated only once a month,  $\text{FF}'_{\text{corr}}$  has small, finite values corresponding to short timescale correlations. The anomalous advection term can now be written out as:

$$(\mathbf{u} \cdot \nabla T')' = \bar{\mathbf{u}} \cdot \nabla T' + \tilde{\mathbf{u}} \cdot \nabla T' + \mathbf{u}' \cdot \nabla \bar{T} + \mathbf{u}' \cdot \nabla \tilde{T} + (\mathbf{u}' \cdot \nabla T')'. \quad (9)$$

To simplify the expression of small terms that are not of interest, we define a seasonal cycle advection term such that  $\text{Adv}'_{\text{SC}} (\equiv -\tilde{\mathbf{u}} \cdot \nabla T' - \mathbf{u}' \cdot \nabla \tilde{T})$ . This makes the anomalous energy budget:

$$\frac{\partial}{\partial t}T'(\mathbf{x}, t) = -\mathbf{u}' \cdot \nabla \bar{T} - \bar{\mathbf{u}} \cdot \nabla T' - (\mathbf{u}' \cdot \nabla T')' + \text{Adv}'_{\text{SC}} + \text{FF}'_{\text{corr}} + \frac{\partial}{\partial z}F'_{\text{SGS}}.$$

Next, we take the volume integral over the equatorial East Pacific upper ocean, defined as the region between  $\sim 205$  and  $263^\circ\text{E}$ , within  $\sim 5$  degrees of the equator, and the top  $\sim 80$  m. These bounds are approximate as the spatial integration is conducted on the native cubed sphere grid. Denoting the volume average of a variable as  $\langle \cdot \rangle = \int \int \int \cdot dx dy dz / (\Delta_x \Delta_y \Delta_z)$ , where  $\Delta_x$ ,  $\Delta_y$ , and  $\Delta_z$  correspond to the zonal, meridional, and vertical distance across the box studied:

$$\frac{d}{dt}\langle T' \rangle = -\langle \bar{\mathbf{u}} \cdot \nabla T' \rangle - \langle \mathbf{u}' \cdot \nabla \bar{T} \rangle - \langle (\mathbf{u}' \cdot \nabla T')' \rangle + \langle \text{Adv}'_{\text{SC}} + \text{FF}'_{\text{corr}} \rangle + \left\langle \frac{\partial}{\partial z}F'_{\text{SGS}} \right\rangle.$$

For the SGS forcings, we evaluate the vertical integral and neglect mixing at the bottom (due to the relatively slow speed of interior ocean mixing [46]), so  $\langle \partial F'_{\text{SGS}} / \partial z \rangle = \langle F' \rangle_{2\text{D}, \text{surf}}$  where  $\langle \cdot \rangle_{2\text{D}, \text{surf}}$  indicates the area average at the ocean's surface and  $F' = \text{SH}' + \text{LH}' + \text{LWR}'$  represents the sum of sensible heat, latent heat, and long-wave radiation (shortwave radiation has no anomalous contribution in the MITgcm, all terms in K/s).

As we wish to understand how the mean climate and anomalous temperatures interact, we assume that net anomalous surface fluxes (including radiation) are proportional to anomalous surface temperature via a slowly changing constant  $\bar{\alpha}_{\text{SF}}$ . This assumption is equivalent to treating surface fluxes as a damping term for ENSO anomalies, as is often done when analyzing ENSO energy budgets [such as when calculating the Bjerknes index, 22, 27, 31]. The budget is now:

$$\frac{d}{dt}\langle T' \rangle = -\langle \bar{\mathbf{u}} \cdot \nabla T' \rangle - \langle \mathbf{u}' \cdot \nabla \bar{T} \rangle - \langle (\mathbf{u}' \cdot \nabla T')' \rangle + \langle \text{Adv}'_{\text{SC}} + \text{FF}'_{\text{corr}} \rangle - \bar{\alpha}_{\text{SF}} \langle T' \rangle_{2\text{D},\text{surf}} \quad (10)$$

where  $\bar{\alpha}_{\text{SF}}$  is calculated as the proportionality constant between  $\langle T' \rangle_{2\text{D},\text{surf}}$  and  $\langle F' \rangle_{2\text{D},\text{surf}}$  across positive values of  $\langle T' \rangle_{2\text{D},\text{surf}}$  within 10 years of time  $t$  (see Extended Data Fig. 3 and Supplementary Text 1 for discussion of this assumption and how  $\bar{\alpha}_{\text{SF}}$  changes with warming).

We test our budget by applying Eq. 10 to a random time interval in Supplemental Fig. S3. The budget for this sample time series (panel a) is mostly closed, and across all time points the budget prediction and simulated tendency are very well correlated (b). There are residuals at some times, likely associated with model output being monthly.

We can also apply East Pacific energy balance to a composite El Niño event in order to understand how ENSO events grow. We create a composite by first identifying the 25 largest values of  $\langle T' \rangle$  divided by the moving East Pacific standard deviation. This normalization is necessary so that the peaks identified are spread out across climates, rather than concentrated in climates with larger ENSO variability. Large values within two years of each other are ignored. The identified events are then composited according to a time relative to the El Niño peak  $\tau$  (defined such that the maximum  $\langle T' \rangle$  is at  $\tau = 0$ ). In other words, a variable at a given  $\tau$  represents the average of that quantity across a set of El Niño events a certain number of months before those events peak. The resulting composited time series from the reference simulation and the relevant energy budget terms are shown in Supplemental Fig. S3c. The budget predicted tendency (solid black line) and the simulated tendency (dashed black line) match well, except for a difference when the tendency is quickly changing around  $\tau = -1$  month. To understand El Niño growth we integrate each term over the buildup to the maximum  $\langle T' \rangle$  value; temperature increases are dominated by anomalous upwelling acting on mean stratification while sub-grid-scale processes (surface fluxes and radiation) damp temperature anomalies significantly (d). The other terms, especially seasonal advection and the flux form correction, are smaller.

We now have a clear expression for changes to East Pacific anomalous temperature, and we wish to transform it into an expression for ENSO variability. The next step is to divide both sides of the budget by  $\langle T' \rangle$ :

$$\frac{1}{\langle T' \rangle} \frac{d}{d\tau} \langle T' \rangle = \left[ -\frac{\langle \bar{\mathbf{u}} \cdot \nabla T' \rangle}{\langle T' \rangle} - \frac{\langle \mathbf{u}' \cdot \nabla \bar{T} \rangle}{\langle T' \rangle} - \frac{\langle (\mathbf{u}' \cdot \nabla T')' \rangle}{\langle T' \rangle} + \frac{\langle \text{Adv}'_{\text{SC}} + \text{FF}'_{\text{corr}} \rangle}{\langle T' \rangle} - \bar{\alpha}_{\text{SF}} \frac{\langle T' \rangle_{2\text{D},\text{surf}}}{\langle T' \rangle} \right]$$

so that the tendency contributions include ratios between two anomalous quantities and therefore are not sensitive to the amplitude of ENSO, but instead express the structure of an ENSO event. By integrating over time, this budget can now be used to diagnose how much  $\langle T' \rangle$  will increase in the lead up to an individual El Niño event. We use a 4th order Runge-Kutta method and integrate from the initiation of an ENSO event at  $\tau = \tau_0$  to its peak time  $\tau = 0$ . The resulting predicted amplitude of an ENSO peak is:

$$\langle T' \rangle_{\text{pred}} = \langle T' \rangle_{\tau_0} \exp \left[ \int_{\tau_0}^0 d\tau \left( -\frac{\langle \bar{\mathbf{u}} \cdot \nabla T' \rangle}{\langle T' \rangle} - \frac{\langle \mathbf{u}' \cdot \nabla \bar{T} \rangle}{\langle T' \rangle} - \frac{\langle \mathbf{u}' \cdot \nabla T' \rangle}{\langle T' \rangle} + \frac{\langle \text{Adv}'_{\text{SC}} + \text{FF}'_{\text{corr}} \rangle}{\langle T' \rangle} - \bar{\alpha}_{\text{SF}} \frac{\langle T' \rangle_{2\text{D,surf}}}{\langle T' \rangle} \right) \right]. \quad (11)$$

In order to avoid  $\langle T' \rangle = 0$ , we define the initiation as the first time when  $\langle T' \rangle$  is larger than 0.125 K for composites or 1 K for individual events, which are noisier. Extended Data Fig. 6 plots the simulated maximum values of  $\langle T' \rangle$  against those diagnosed by this equation; the predictions match the simulations with an  $R^2$  of 0.85 and a slope very close to 1.

### Predicting ENSO Magnitude in a Changing Climate

We will now use Eq. 11 to understand how and why El Niño events change with the mean climate (i.e., as  $\bar{\mathbf{u}}$ ,  $\nabla \bar{T}$ , and  $\bar{\alpha}_{\text{SF}}$  evolve). As before, 25 identified El Niño events from the control simulation are used to create composite quantities as a function of time  $\tau$ . For each event, a time relative to the peak is defined such that  $\langle T' \rangle$  is at its maximum value when  $\tau = 0$ , then averages are taken at each value of  $\tau$  across the 25 identified events to calculate  $\mathbf{u}'(\mathbf{x}, \tau)/\langle T' \rangle(\tau)$ ,  $\nabla T'(\mathbf{x}, \tau)/\langle T' \rangle(\tau)$ , and  $\langle T' \rangle_{2\text{D,surf}}(\tau)/\langle T' \rangle(\tau)$ . These three variables represent the characteristic structure of an El Niño event and are assumed to be constant with warming (discussed below). We can then use energy balance at any time  $t$  to study how  $\langle T' \rangle$  grows during an El Niño event in that climate. In other words, we represent a mean climate with  $\bar{\mathbf{u}}$ ,  $\nabla \bar{T}$ , and  $\bar{\alpha}_{\text{SF}}$  as a function of  $t$  and place a composite El Niño structure represented by  $\mathbf{u}'/\langle T' \rangle$ ,  $\nabla T'/\langle T' \rangle$ , and  $\langle T' \rangle_{2\text{D,surf}}/\langle T' \rangle$  as a function of  $\tau$  in that climate. The peak amplitude resulting from an El Niño event in that chosen climate is:

$$\langle T' \rangle_{\text{pred}}(t) = \langle T' \rangle_{\tau_0} \exp \left[ \int_{\tau_0}^0 d\tau \left( -\frac{\langle \bar{\mathbf{u}} \cdot \nabla T' \rangle}{\langle T' \rangle} - \frac{\langle \mathbf{u}'_h \cdot \nabla_h \bar{T} \rangle}{\langle T' \rangle} - \frac{\langle w' \bar{\Gamma} \rangle}{\langle T' \rangle} - \bar{\alpha}_{\text{SF}} \frac{\langle T' \rangle_{2\text{D,surf}}}{\langle T' \rangle} \right) \right] \quad (12)$$

where the non-linear terms and flux form correction have been ignored here for convenience but are included in the calculations for Fig. 3 and the mean stratification ( $\bar{\Gamma}$ ) is separated because it drives the ENSO variability increase. This is the same equation as above, but now all anomalous variables come from an El Niño composite in the control simulation while the mean variables come from a changing climate. For example, in the stratification term ( $\langle w' \bar{\Gamma} \rangle / \langle T' \rangle$ ) we use the anomalous upwelling per degree anomalous East Pacific temperature ( $w' / \langle T' \rangle$ ) from the reference climate and keep this constant as  $t$  changes, but allow the mean stratification ( $\bar{\Gamma}$ ) to evolve. Similarly, for the surface fluxes,  $\langle T' \rangle_{2\text{D,surf}} / \langle T' \rangle$  is assumed to be constant as the climate

warms, but  $\bar{\alpha}_{\text{SF}}$  changes. This equation uses the El Niño event structure from a reference climate and mean climate variables at a given time  $t$  to predict the buildup to an El Niño peak if one had happened in that climate. The result is a predicted maximum temperature anomaly as a function of  $t$ , which changes as the climate warms, i.e., with  $\bar{\mathbf{u}}(t)$ ,  $\nabla\bar{T}(t)$ , and  $\bar{\alpha}_{\text{SF}}(t)$ . Additionally, this equation can be evaluated with only one mean variable changing over time, allowing for the calculation of contributions from each term to changes in ENSO peaks (Fig. 3d).

In order to use Eq. 12 to predict  $\Delta M_{\text{ENSO}}$ , we divide both sides by their equivalent reference simulation expression and subtract one, giving:

$$\frac{\langle T'_{\text{pred}} \rangle}{\langle T'_{\text{pred,ctrl}} \rangle} - 1 = \frac{\exp \left[ \int_{\tau_0}^0 d\tau \left( -\frac{\langle \bar{\mathbf{u}} \cdot \nabla T' \rangle}{\langle T' \rangle} - \frac{\langle \mathbf{u}'_h \cdot \nabla_h \bar{T} \rangle}{\langle T' \rangle} - \frac{\langle w' \bar{\Gamma} \rangle}{\langle T' \rangle} - \bar{\alpha}_{\text{SF}} \frac{\langle T' \rangle_{2\text{D},\text{surf}}}{\langle T' \rangle} \right) \right]}{\exp \left[ \int_{\tau_0}^0 d\tau \left( -\frac{\langle \bar{\mathbf{u}}_{\text{ctrl}} \cdot \nabla T' \rangle}{\langle T' \rangle} - \frac{\langle \mathbf{u}'_h \cdot \nabla_h \bar{T}_{\text{ctrl}} \rangle}{\langle T' \rangle} - \frac{\langle w' \bar{\Gamma}_{\text{ctrl}} \rangle}{\langle T' \rangle} - \bar{\alpha}_{\text{SF,ctrl}} \frac{\langle T' \rangle_{2\text{D},\text{surf}}}{\langle T' \rangle} \right) \right]} - 1. \quad (13)$$

Next, we define  $\Delta$  terms as differences from control simulation values (e.g.,  $\Delta \bar{\mathbf{u}} = \bar{\mathbf{u}} - \bar{\mathbf{u}}_{\text{ctrl}}$ ), and the reference terms are moved into the same exponential as the original expression. Lastly, we assume that the normalized ENSO magnitude represented by  $\frac{\langle T'_{\text{pred}} \rangle}{\langle T'_{\text{pred,ctrl}} \rangle} - 1$  is equal to the normalized ENSO magnitude used in the main text (Extended Data Fig. 2). Our final energy balance prediction is therefore:

$$\Delta M_{\text{ENSO}} = \exp \left[ \int_{\tau_0}^0 d\tau \left( -\frac{\langle \Delta \bar{\mathbf{u}} \cdot \nabla T' \rangle}{\langle T' \rangle} - \frac{\langle \mathbf{u}'_h \cdot \Delta \nabla_h \bar{T} \rangle}{\langle T' \rangle} - \frac{w' \Delta \Gamma}{\langle T' \rangle} - \Delta \bar{\alpha}_{\text{SF}} \frac{\langle T' \rangle_{2\text{D},\text{surf}}}{\langle T' \rangle} \right) \right] - 1. \quad (14)$$

Eq. 14 is the final expression used to predict ENSO magnitude in Fig. 3 and is a robust and flexible way to understand how changes in climate affect ENSO peaks. However, this method assumes changes to the structure of El Niño events, i.e., the spatial and  $\tau$  dependence of quantities such as  $w'/\langle T' \rangle$ , do not significantly alter the magnitude of ENSO as the climate warms. This is a common assumption in the study of ENSO [26, 27, 31], and is necessary due to the difficulty of predicting the precise structure of the anomaly variables over time. We now assess the validity of this assumption by first displaying ENSO structures over time then directly evaluating how changes in structure alter the predicted amplitude.

The time-dependent structure of a composite ENSO anomaly is shown in Fig. S4. Although there is some noise, the volume average anomalous quantities as a function of  $\tau$  are not significantly different in a warmer climate from those of the reference climate (panel a). Additionally, the spatial structure of normalized anomalous quantities are similar in the control and warmed climate (panel b), although the temperature anomaly becomes more concentrated near the surface. These similar structures with respect to  $\tau$  and space lead to good correlations between anomalous variables in the control and warmed climates (panel c), although  $w'$  is somewhat noisy. Lastly, the anomalous variables as a function of time tend to stay within 20% of their reference value (d), though there is some movement.

We more directly assess the importance of ENSO structure changes by evaluating Eq. 14 using different ENSO composites and seeing how the results differ (Extended Data Fig. 7). Using composites from the control or warmed state gives very similar time series, and changing one anomaly variable at a time also has little impact. The exception is  $w'$ , for which the warmed version leads to somewhat smaller ENSO events during the phase of enhanced variability. Comparing the control and warmed structure results directly has an  $R^2$  value of 0.98 (panel b), showing that overall, changes to ENSO structure with warming play only a minor role in setting its amplitude, validating our use of a constant El Niño structure over time.

## References

- [1] Adams, R.M., Chen, C.-C., McCarl, B.A., Weiher, R.F.: The economic consequences of ENSO events for agriculture **13**, 165–172 <https://doi.org/10.3354/cr013165> . Accessed 2025-08-08
- [2] Liu, Y., Cai, W., Lin, X., Li, Z., Zhang, Y.: Nonlinear el niño impacts on the global economy under climate change **14**(1), 5887 <https://doi.org/10.1038/s41467-023-41551-9> . Publisher: Nature Publishing Group. Accessed 2025-08-08
- [3] Hamlet, A.F., Lettenmaier, D.P.: Effects of 20th century warming and climate variability on flood risk in the western u.s. **43**(6) <https://doi.org/10.1029/2006WR005099> . \_eprint: <https://agupubs.onlinelibrary.wiley.com/doi/pdf/10.1029/2006WR005099>. Accessed 2025-08-08
- [4] Lin, I.-I., Camargo, S.J., Patricola, C.M., Boucharel, J., Chand, S., Klotzbach, P., Chan, J.C.L., Wang, B., Chang, P., Li, T., Jin, F.-F.: ENSO and tropical cyclones. In: El Niño Southern Oscillation in a Changing Climate, pp. 377–408. American Geophysical Union (AGU). <https://doi.org/10.1002/9781119548164.ch17> . Section: 17 \_eprint: <https://agupubs.onlinelibrary.wiley.com/doi/pdf/10.1002/9781119548164.ch17>. <https://onlinelibrary.wiley.com/doi/abs/10.1002/9781119548164.ch17> Accessed 2025-08-08
- [5] Callahan, C.W., Mankin, J.S.: Persistent effect of el niño on global economic growth **380**(6649), 1064–1069 <https://doi.org/10.1126/science.adf2983> . Publisher: American Association for the Advancement of Science. Accessed 2025-05-08
- [6] Battisti, D.S., Sarachik, E.S.: Understanding and predicting ENSO **33**(52), 1367–1376. Accessed 2024-06-20
- [7] McPhaden, M.J., Zebiak, S.E., Glantz, M.H.: ENSO as an integrating concept in earth science **314**(5806), 1740–1745 <https://doi.org/10.1126/science.1132588> . Publisher: American Association for the Advancement of Science. Accessed 2025-05-06
- [8] Timmermann, A., An, S.-I., Kug, J.-S., Jin, F.-F., Cai, W., Capotondi, A., Cobb, K.M., Lengaigne, M., McPhaden, M.J., Stuecker, M.F., Stein, K., Wittenberg, A.T., Yun, K.-S., Bayr, T., Chen, H.-C., Chikamoto, Y., Dewitte, B., Dommenges, D., Grothe, P., Guilyardi, E., Ham, Y.-G., Hayashi, M., Ineson, S., Kang, D., Kim, S., Kim, W., Lee, J.-Y., Li, T., Luo, J.-J., McGregor, S., Planton, Y., Power, S., Rashid, H., Ren, H.-L., Santoso, A., Takahashi, K., Todd, A., Wang, G., Wang, G., Xie, R., Yang, W.-H., Yeh, S.-W., Yoon, J., Zeller, E., Zhang, X.: El niño–southern oscillation complexity **559**(7715), 535–545 <https://doi.org/10.1038/s41586-018-0252-6> . Number: 7715 Publisher: Nature Publishing Group.

Accessed 2024-02-09

- [9] Fedorov, A.V., Philander, S.G.: Is el niño changing? **288**(5473), 1997–2002 <https://doi.org/10.1126/science.288.5473.1997> . Publisher: American Association for the Advancement of Science. Accessed 2024-02-09
- [10] Latif, M., Keenlyside, N.S.: El niño/southern oscillation response to global warming **106**(49), 20578–20583 <https://doi.org/10.1073/pnas.0710860105> . Publisher: Proceedings of the National Academy of Sciences. Accessed 2025-04-20
- [11] Guilyardi, E., Wittenberg, A., Fedorov, A., Collins, M., Wang, C., Capotondi, A., Oldenborgh, G.J.v., Stockdale, T.: Understanding el niño in ocean–atmosphere general circulation models: Progress and challenges **90**(3), 325–340 <https://doi.org/10.1175/2008BAMS2387.1> . Publisher: American Meteorological Society Section: Bulletin of the American Meteorological Society. Accessed 2023-10-19
- [12] Hersbach, H., Bell, B., Berrisford, P., Hirahara, S., Horányi, A., Muñoz-Sabater, J., Nicolas, J., Peubey, C., Radu, R., Schepers, D., Simmons, A., Soci, C., Abdalla, S., Abellan, X., Balsamo, G., Bechtold, P., Biavati, G., Bidlot, J., Bonavita, M., De Chiara, G., Dahlgren, P., Dee, D., Diamantakis, M., Dragani, R., Flemming, J., Forbes, R., Fuentes, M., Geer, A., Haimberger, L., Healy, S., Hogan, R.J., Hólm, E., Janisková, M., Keeley, S., Laloyaux, P., Lopez, P., Lupu, C., Radnoti, G., Rosnay, P., Rozum, I., Vamborg, F., Villaume, S., Thépaut, J.-N.: The ERA5 global reanalysis. *Quarterly Journal of the Royal Meteorological Society* **146**(730), 1999–2049 (2020) <https://doi.org/10.1002/qj.3803> . eprint: <https://onlinelibrary.wiley.com/doi/pdf/10.1002/qj.3803>. Accessed 2022-03-29
- [13] Cai, W., Santoso, A., Collins, M., Dewitte, B., Karamperidou, C., Kug, J.-S., Lengaigne, M., McPhaden, M.J., Stuecker, M.F., Taschetto, A.S., Timmermann, A., Wu, L., Yeh, S.-W., Wang, G., Ng, B., Jia, F., Yang, Y., Ying, J., Zheng, X.-T., Bayr, T., Brown, J.R., Capotondi, A., Cobb, K.M., Gan, B., Geng, T., Ham, Y.-G., Jin, F.-F., Jo, H.-S., Li, X., Lin, X., McGregor, S., Park, J.-H., Stein, K., Yang, K., Zhang, L., Zhong, W.: Changing el niño–southern oscillation in a warming climate **2**(9), 628–644 <https://doi.org/10.1038/s43017-021-00199-z> . Number: 9 Publisher: Nature Publishing Group. Accessed 2024-02-09
- [14] Gan, R., Liu, Q., Huang, G., Hu, K., Li, X.: Greenhouse warming and internal variability increase extreme and central pacific el niño frequency since 1980 **14**(1), 394 <https://doi.org/10.1038/s41467-023-36053-7> . Publisher: Nature Publishing Group. Accessed 2024-06-17
- [15] Cai, W., Wang, G., Dewitte, B., Wu, L., Santoso, A., Takahashi, K., Yang, Y., Carréric, A., McPhaden, M.J.: Increased variability of eastern pacific el niño under greenhouse warming **564**(7735), 201–206 <https://doi.org/10.1038/s41586-018-0776-9> . Publisher: Nature Publishing Group. Accessed 2024-06-17

- [16] Cai, W., Wang, G., Santoso, A., McPhaden, M.J., Wu, L., Jin, F.-F., Timmermann, A., Collins, M., Vecchi, G., Lengaigne, M., England, M.H., Dommenget, D., Takahashi, K., Guilyardi, E.: Increased frequency of extreme la niña events under greenhouse warming **5**(2), 132–137 <https://doi.org/10.1038/nclimate2492> . Publisher: Nature Publishing Group. Accessed 2024-06-17
- [17] Wang, G., Cai, W., Gan, B., Wu, L., Santoso, A., Lin, X., Chen, Z., McPhaden, M.J.: Continued increase of extreme el niño frequency long after 1.5 °c warming stabilization **7**(8), 568–572 <https://doi.org/10.1038/nclimate3351> . Publisher: Nature Publishing Group. Accessed 2024-06-17
- [18] Kim, S.T., Cai, W., Jin, F.-F., Santoso, A., Wu, L., Guilyardi, E., An, S.-I.: Response of el niño sea surface temperature variability to greenhouse warming **4**(9), 786–790 <https://doi.org/10.1038/nclimate2326> . Publisher: Nature Publishing Group. Accessed 2025-09-09
- [19] Peng, Q., Xie, S.-P., Deser, C.: Collapsed upwelling projected to weaken ENSO under sustained warming beyond the twenty-first century, 1–8 <https://doi.org/10.1038/s41558-024-02061-8> . Publisher: Nature Publishing Group. Accessed 2024-07-09
- [20] Geng, T., Cai, W., Jia, F., Wu, L.: Decreased ENSO post-2100 in response to formation of a permanent el niño-like state under greenhouse warming **15**(1), 5810 <https://doi.org/10.1038/s41467-024-50156-9> . Publisher: Nature Publishing Group. Accessed 2025-04-20
- [21] Callahan, C.W., Chen, C., Rugenstein, M., Bloch-Johnson, J., Yang, S., Moyer, E.J.: Robust decrease in el niño/southern oscillation amplitude under long-term warming **11**(9), 752–757 <https://doi.org/10.1038/s41558-021-01099-2> . Publisher: Nature Publishing Group. Accessed 2024-06-17
- [22] Tuckman, P.J.: Understanding ENSO weakening in warmer climates **52**(11), 2024–113124 <https://doi.org/10.1029/2024GL113124> . eprint: <https://agupubs.onlinelibrary.wiley.com/doi/pdf/10.1029/2024GL113124>. Accessed 2025-06-22
- [23] Eyring, V., Bony, S., Meehl, G.A., Senior, C.A., Stevens, B., Stouffer, R.J., Taylor, K.E.: Overview of the Coupled Model Intercomparison Project Phase 6 (CMIP6) experimental design and organization. *Geoscientific Model Development* **9**(5), 1937–1958 (2016) <https://doi.org/10.5194/gmd-9-1937-2016> . Publisher: Copernicus GmbH. Accessed 2022-09-01
- [24] Kay, J.E., Wall, C., Yettella, V., Medeiros, B., Hannay, C., Caldwell, P., Bitz, C.: Global climate impacts of fixing the southern ocean shortwave radiation bias in the community earth system model (CESM) **29**(12), 4617–4636 <https://doi.org/10.1175/JCLI-D-15-0358.1> . Publisher: American Meteorological Society Section: Journal of Climate. Accessed 2024-11-07

- [25] Marshall, J., Adcroft, A., Hill, C., Perelman, L., Heisey, C.: A finite-volume, incompressible navier stokes model for studies of the ocean on parallel computers **102**, 5753–5766 <https://doi.org/10.1029/96JC02775> . eprint: <https://onlinelibrary.wiley.com/doi/pdf/10.1029/96JC02775>. Accessed 2022-03-17
- [26] Tuckman, P.J., Smyth, J.E., Li, J., Lutsko, N.J., Marshall, J.: ENSO and west pacific seasonality driven by the south asian monsoon **52**(9), 2024–111084 <https://doi.org/10.1029/2024GL111084> . eprint: <https://onlinelibrary.wiley.com/doi/pdf/10.1029/2024GL111084>. Accessed 2025-05-04
- [27] Jin, F.-F., Kim, S.T., Bejarano, L.: A coupled-stability index for ENSO **33**(23) <https://doi.org/10.1029/2006GL027221> . eprint: <https://onlinelibrary.wiley.com/doi/pdf/10.1029/2006GL027221>. Accessed 2023-02-07
- [28] Meehl, G.A., Washington, W.M.: El niño-like climate change in a model with increased atmospheric CO<sub>2</sub> concentrations **382**(6586), 56–60 <https://doi.org/10.1038/382056a0> . Publisher: Nature Publishing Group. Accessed 2024-06-17
- [29] Vecchi, G.A., Soden, B.J.: Global warming and the weakening of the tropical circulation **20**(17), 4316–4340 <https://doi.org/10.1175/JCLI4258.1> . Publisher: American Meteorological Society Section: Journal of Climate. Accessed 2024-06-17
- [30] Wills, R.C., Levine, X.J., Schneider, T.: Local Energetic Constraints on Walker Circulation Strength. *Journal of the Atmospheric Sciences* **74**(6), 1907–1922 (2017) <https://doi.org/10.1175/JAS-D-16-0219.1> . Publisher: American Meteorological Society Section: Journal of the Atmospheric Sciences. Accessed 2023-04-13
- [31] Jin, F.-F., Chen, H.-C., Zhao, S., Hayashi, M., Karamperidou, C., Stuecker, M.F., Xie, R., Geng, L.: Simple ENSO models. In: *El Niño Southern Oscillation in a Changing Climate*, pp. 119–151. American Geophysical Union (AGU). <https://doi.org/10.1002/9781119548164.ch6> . Section: 6 eprint: <https://onlinelibrary.wiley.com/doi/pdf/10.1002/9781119548164.ch6>. <https://onlinelibrary.wiley.com/doi/abs/10.1002/9781119548164.ch6> Accessed 2024-06-20
- [32] McCreary, J.P., Lu, P.: Interaction between the subtropical and equatorial ocean circulations: The subtropical cell **24**(2), 466–497 [https://doi.org/10.1175/1520-0485\(1994\)024<0466:IBTSAE>2.0.CO;2](https://doi.org/10.1175/1520-0485(1994)024<0466:IBTSAE>2.0.CO;2) . Publisher: American Meteorological Society Section: Journal of Physical Oceanography. Accessed 2024-11-17
- [33] Liu, Z., Philander, S.G.H., Pacanowski, R.C.: A GCM Study of Tropical–Subtropical Upper-Ocean Water Exchange (1994). Section: *Journal of Physical Oceanography*. Accessed 2025-05-07

- [34] Clement, A.C., Seager, R., Cane, M.A., Zebiak, S.E.: An ocean dynamical thermostat. *Journal of Climate* **9**(9), 2190–2196 (1996)
- [35] Vecchi, G.A., Clement, A., Soden, B.J.: Examining the tropical pacific’s response to global warming **89**(9), 81–83 <https://doi.org/10.1029/2008EO090002> . eprint: <https://onlinelibrary.wiley.com/doi/pdf/10.1029/2008EO090002>. Accessed 2024-11-13
- [36] Seager, R., Cane, M., Henderson, N., Lee, D.-E., Abernathey, R., Zhang, H.: Strengthening tropical pacific zonal sea surface temperature gradient consistent with rising greenhouse gases **9**(7), 517–522 <https://doi.org/10.1038/s41558-019-0505-x> . Publisher: Nature Publishing Group. Accessed 2024-06-17
- [37] Zhou, C., Zelinka, M.D., Dessler, A.E., Wang, M.: Greater committed warming after accounting for the pattern effect. *Nature Climate Change* **11**(2), 132–136 (2021)
- [38] Dong, Y., Armour, K.C., Zelinka, M.D., Proistosescu, C., Battisti, D.S., Zhou, C., Andrews, T.: Intermodel spread in the pattern effect and its contribution to climate sensitivity in cmip5 and cmip6 models. *Journal of Climate* **33**(18), 7755–7775 (2020)
- [39] Rodgers, K.B., Lee, S.-S., Rosenbloom, N., Timmermann, A., Danabasoglu, G., Deser, C., Edwards, J., Kim, J.-E., Simpson, I.R., Stein, K., Stuecker, M.F., Yamaguchi, R., Bódai, T., Chung, E.-S., Huang, L., Kim, W.M., Lamarque, J.-F., Lombardozzi, D.L., Wieder, W.R., Yeager, S.G.: Ubiquity of human-induced changes in climate variability **12**(4), 1393–1411 <https://doi.org/10.5194/esd-12-1393-2021> . Publisher: Copernicus GmbH. Accessed 2025-07-09
- [40] Lee, J.-Y., Marotzke, J., Bala, G., Cao, L., Corti, S., Dunne, J.P., Engelbrecht, F., Fischer, E., Fyfe, J.C., Jones, C., et al.: Future global climate: scenario-based projections and near-term information (2021)
- [41] Tuckman, P.J., Smyth, J., Lutsko, N.J., Marshall, J.: The zonal seasonal cycle of tropical precipitation: Introducing the indo-pacific monsoonal mode -1 <https://doi.org/10.1175/JCLI-D-23-0125.1> . Publisher: American Meteorological Society Section: *Journal of Climate*. Accessed 2024-04-10
- [42] Adcroft, A., Campin, J.-M., Hill, C., Marshall, J.: Implementation of an atmosphere–ocean general circulation model on the expanded spherical cube **132**(12), 2845–2863 <https://doi.org/10.1175/MWR2823.1> . Publisher: American Meteorological Society Section: *Monthly Weather Review*. Accessed 2022-03-21
- [43] Frierson, D.M.W., Held, I.M., Zurita-Gotor, P.: A gray-radiation aquaplanet moist GCM. part II: Energy transports in altered climates **64**(5), 1680–1693 <https://doi.org/10.1175/JAS3913.1> . Publisher: American Meteorological Society Section: *Journal of the Atmospheric Sciences*. Accessed 2022-03-21

- [44] Byrne, M.P., O’Gorman, P.A.: Land–ocean warming contrast over a wide range of climates: Convective quasi-equilibrium theory and idealized simulations **26**(12), 4000–4016 <https://doi.org/10.1175/JCLI-D-12-00262.1> . Publisher: American Meteorological Society Section: Journal of Climate. Accessed 2022-03-21
- [45] Gaspar, P., Grégoris, Y., Lefevre, J.-M.: A simple eddy kinetic energy model for simulations of the oceanic vertical mixing: Tests at station papa and long-term upper ocean study site **95**, 16179–16193 <https://doi.org/10.1029/JC095iC09p16179> . \_eprint: <https://onlinelibrary.wiley.com/doi/pdf/10.1029/JC095iC09p16179>. Accessed 2023-04-24
- [46] Munk, W.H.: Abyssal recipes. In: Deep Sea Research and Oceanographic Abstracts, vol. 13, pp. 707–730 (1966). Elsevier

**Acknowledgements.** We would like to thank the University of Chicago for research support and NCAR for the use of data stored on the Derecho computer system. D. Y. is supported by the NSF Career award and the Packard Fellowship.

## Extended Data Legends

**Extended Data Fig. 1 — Fig. 1 without smoothing.** As in Fig. 1, but values of  $\Delta M_{\text{ENSO}}$  are not smoothed by a 20 year moving mean. Values of  $R^2$  are lower due to more noise and unrelated internal variability: The CMIP ensemble has an  $R^2$  of 0.91, CESM 3-7.0 has an  $R^2$  of 0.86 while all CESM scenarios have an  $R^2$  of 0.52, and MITgcm  $\Delta t = 50$  yr has an  $R^2$  of 0.99 while all MITgcm scenarios have an  $R^2$  of 0.92

**Extended Data Fig. 2 — El Niño peak magnitude and East Pacific standard deviation.** Comparing East Pacific standard deviation to El Niño peak magnitude over time in all MITgcm simulations, and the corresponding  $R^2$  value (0.94)

**Extended Data Fig. 3 — Understanding the change in surface fluxes with warming.** Dependence of surface flux damping and its components on warming. Panel a shows the sum of anomalous radiation and turbulent fluxes (i.e.,  $\langle F' \rangle_{2\text{D},\text{surf}}$ ) as a function of anomalous surface temperature across all MITgcm simulations, with color representing mean temperature. Panel b shows the same, but the temperature lost through only anomalous latent heat flux (LHF) rather than all sub-grid-scale processes. Panel c shows how the relationship between the quantities shown in a and b change over time in the  $\Delta t = 50$  year simulations:  $\bar{\alpha}$  is diagnosed as the slope between an anomalous energy source (or sink) and temperature over a 20 year period for positive values of SST', and the contributions from LHF, sensible heat (SHF), and radiation (LWR), as well as the total  $\bar{\alpha}_{\text{SF}}$ , are shown. Panel d shows the linear components of  $\bar{\alpha}_{\text{LHF}}$  and their sum, while panel e further decomposes the most relevant term into changes due to saturation specific humidity and anomalous relative humidity

**Extended Data Fig. 4 — The Inter-model spread of ENSO's response to warming.** Diagnostics of the intermodel-spread of ENSO's response to warming. The top-left panel shows ENSO strength over time across the CMIP abrupt 4xCO<sub>2</sub> ensemble, while the bottom-left shows this time series normalized by the final warming amount. The top-right shows a histogram of  $\alpha$  diagnosed as the peak ENSO strength divided by temperature change at that time, and the bottom-right shows a histogram of  $\alpha + \beta$  diagnosed as the steady state ENSO change divided by the steady state temperature change (last 20 years assumed to be in steady-state). In the right two panels, the fit values from MITgcm and CESM2 are also indicated

**Extended Data Fig. 5 — Sample temperature trajectories from CESM across SSP scenarios.** Sample temperature trajectories used to predict ENSO, capturing the temperature evolution with a few parameters and how they compare to various scenarios simulated by CESM2

**Extended Data Fig. 6 — Predicted vs. Simulated ENSO Peaks.** The maximum  $T'$  achieved by simulated El Niño peaks compared to those predicted from the budget discussed and the identity line ( $x=y$ , red) as a basis of comparison. 25 El Niño events from each simulation are shown. For this figure  $\tau_0$  is defined as when  $\langle T' \rangle$  crosses 1 K

**Extended Data Fig. 7 — The effect of changing ENSO structure on predicted magnitude.** How using the control or warmed ENSO structure alters ENSO magnitude predictions. The top panel shows the same time series as Fig. 3 but using the control or warmed structure or a mixture (i.e., most variables from the reference composite and one variable from the warmed composite), while the bottom panel shows the relationship between the control and warmed ENSO structure predictions

**Extended Data Fig. 8 — Predicting ENSO Magnitude from calculated and empirically fit parameters.** ENSO magnitude over time, comparing the energy budget approximations given by Eq. 6 (dashed), the empirically fit linear model (dotted), and the full energy budget (solid). For each of the three, the result of changing stratification (red), mean temperature (black), or the full time evolution (green) are shown

**Extended Data Table 1 — Empirically fit vs. energy balance predicted models of ENSO variability.** Comparing empirically fit and predicted parameters for the first linear model applied to the MITgcm. The corresponding time series are shown in Extended Data Fig. 8

Parameter	Empirical fit	Energy budget prediction	Error
A (1/K)	-0.14	-0.15	7%
B (m/K)	7.8	6.6	15%

**Extended Data Table 2 — Fit parameters for each linear model.** Values of the relevant parameters for the two linear models, calculated as discussed in the main text and methods section.

Variable	MITgcm	CESM2-LE	CMIP Ensemble Abrupt
A (1/K)	-0.14		
B (m/K)	7.8		
$\alpha$ (1/K)	0.04	0.21	0.10
$\beta$ (1/K)	-0.07	-0.29	-0.11
$t_{lag}$ (yr)	34.6	28.2	21.5

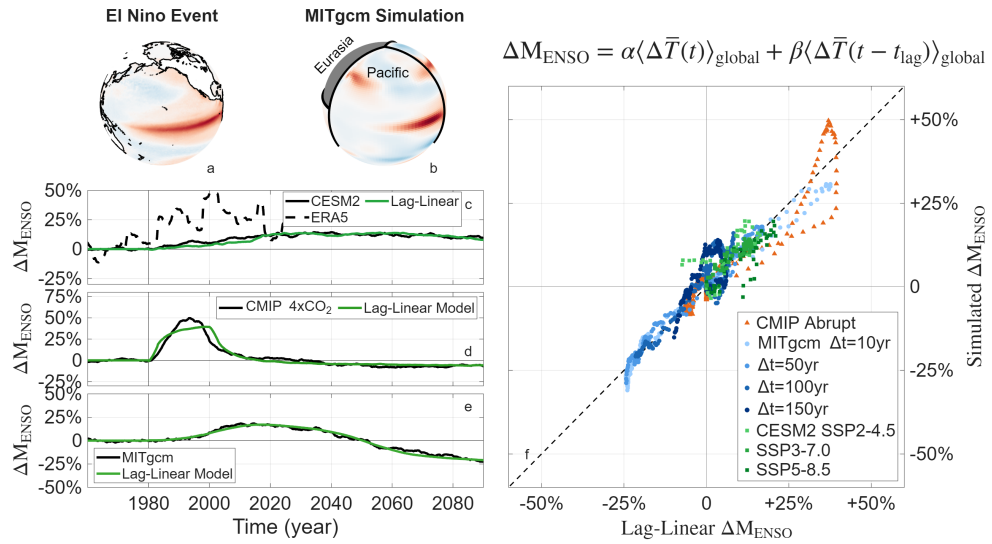
# Extended Data: The Rise and Fall of ENSO in a Warming World: Insights from a Lag-Linear Model

P.J. Tuckman<sup>1\*</sup> and Da Yang<sup>1,2\*</sup>

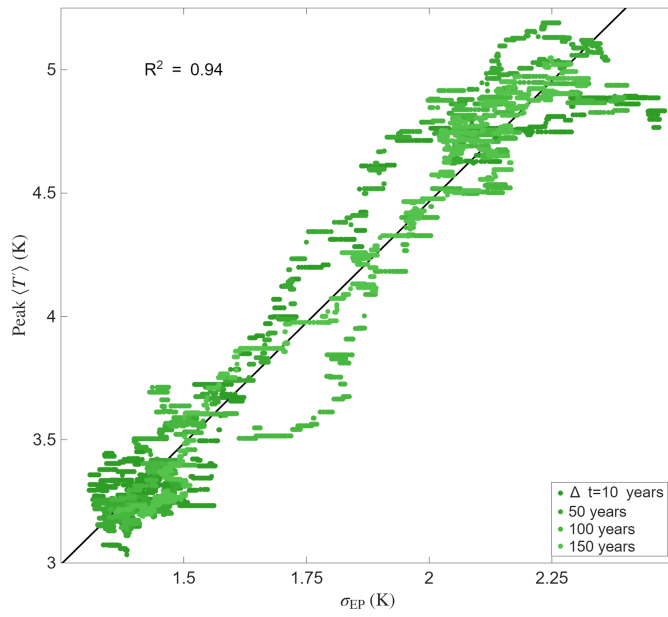
<sup>1</sup>Department of Geophysical Sciences, University of Chicago, 5734 S  
Ellis Ave, Chicago, IL, 60637, United States of America.

<sup>2</sup>Department of Geophysics, Stanford University, 397 Panama Mall,  
Stanford, CA, 94305, United States of America.

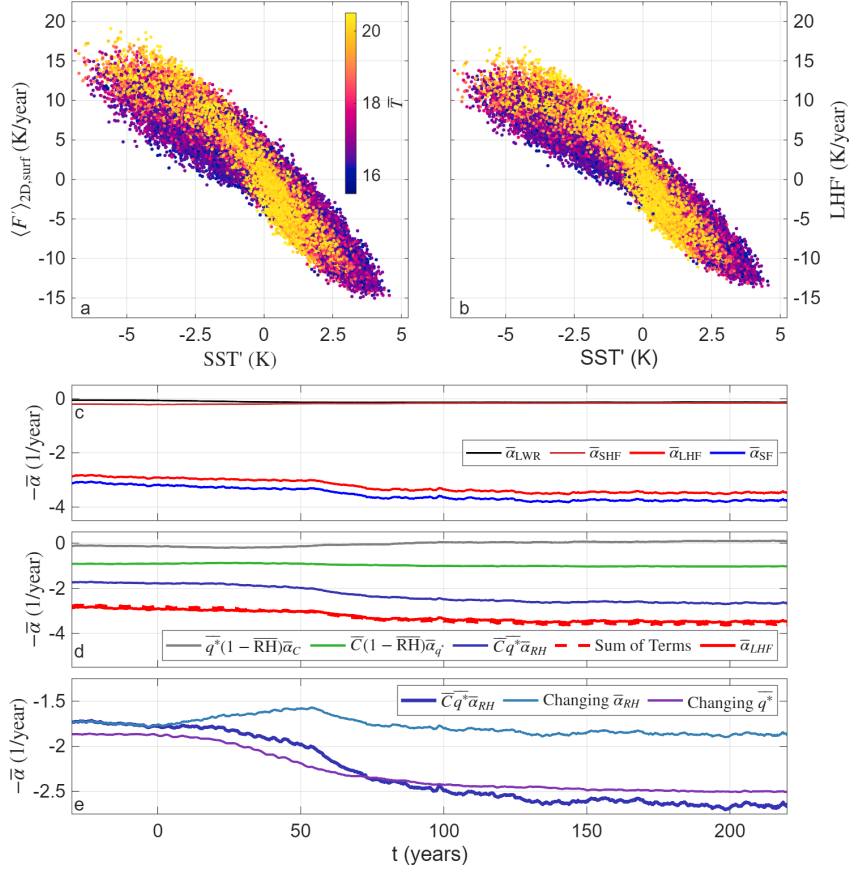
\*Corresponding author(s). E-mail(s): [pjt5@uchicago.edu](mailto:pjt5@uchicago.edu);  
[dayang@stanford.edu](mailto:dayang@stanford.edu);



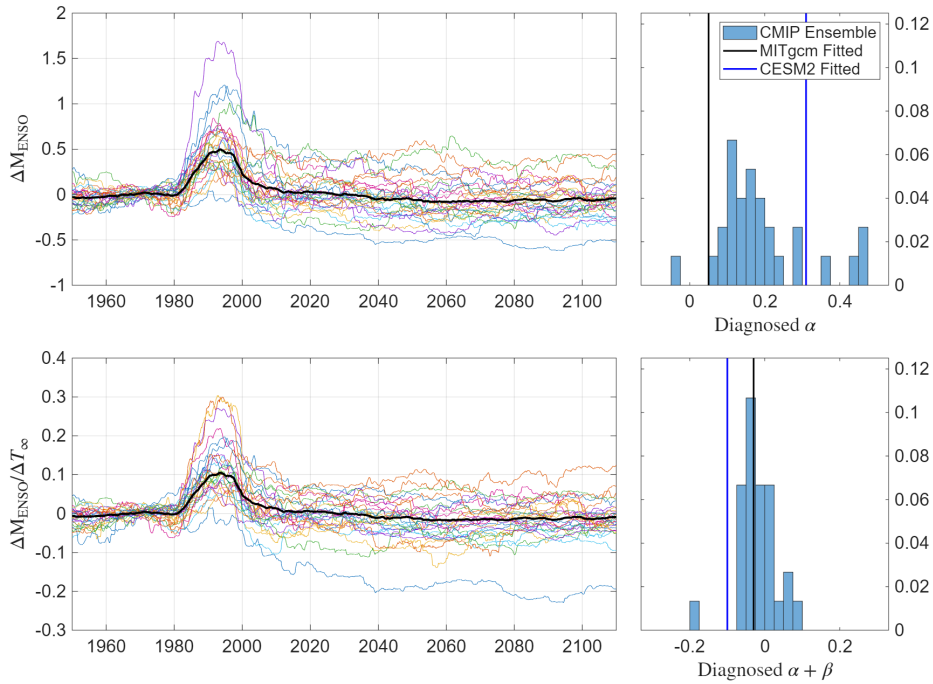
**Extended Data Fig. 1 | Fig. 1 without smoothing.** As in Fig. 1, but values of  $\Delta M_{\text{ENSO}}$  are not smoothed by a 20 year moving mean. Values of  $R^2$  are lower due to more noise and unrelated internal variability: The CMIP ensemble has an  $R^2$  of 0.91, CESM 3-7.0 has an  $R^2$  of 0.86 while all CESM scenarios have an  $R^2$  of 0.52, and MITgcm  $\Delta t = 50$  yr has an  $R^2$  of 0.99 while all MITgcm scenarios have an  $R^2$  of 0.92.



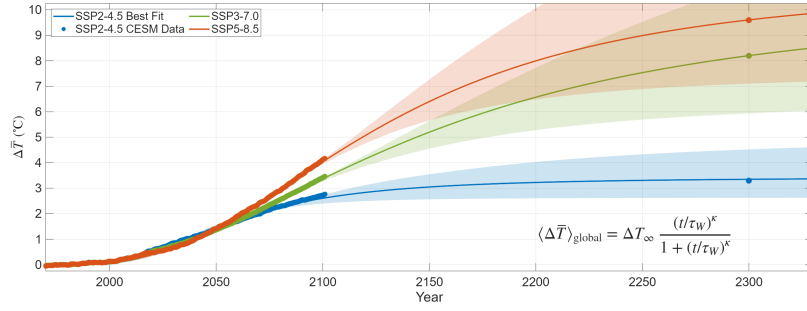
**Extended Data Fig. 2 | El Niño peak magnitude and East Pacific standard deviation.** Comparing East Pacific standard deviation to El Niño peak magnitude over time in all MITgcm simulations, and the corresponding  $R^2$  value (0.94).



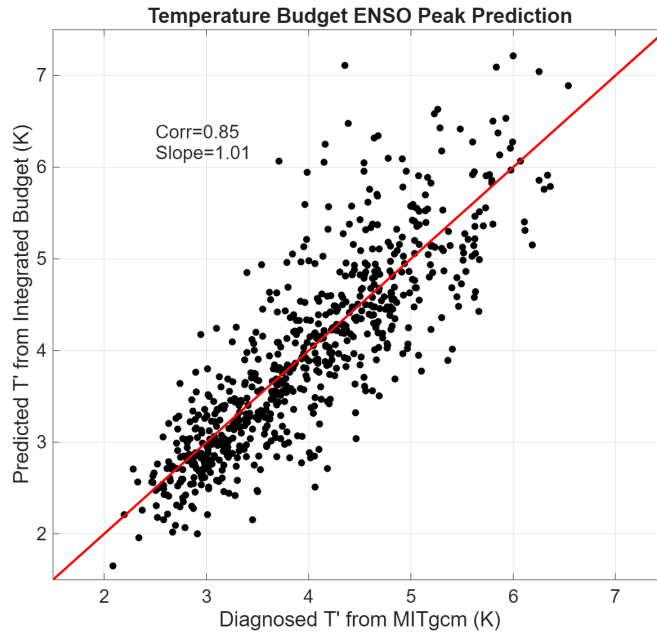
**Extended Data Fig. 3 | Understanding the change in surface fluxes with warming.** Dependence of surface flux damping and its components on warming. Panel a shows the sum of anomalous radiation and turbulent fluxes (i.e.,  $\langle F' \rangle_{2D,surf}$ ) as a function of anomalous surface temperature across all MITgcm simulations, with color representing mean temperature. Panel b shows the same, but the temperature lost through only anomalous latent heat flux (LHF) rather than all sub-grid-scale processes. Panel c shows how the relationship between the quantities shown in a and b change over time in the  $\Delta t = 50$  year simulations:  $\bar{\alpha}$  is diagnosed as the slope between an anomalous energy source (or sink) and temperature over a 20 year period for positive values of SST', and the contributions from LHF, sensible heat (SHF), and radiation (LWR), as well as the total  $\bar{\alpha}_{SF}$ , are shown. Panel d shows the linear components of  $\bar{\alpha}_{LHF}$  and their sum, while panel e further decomposes the most relevant term into changes due to saturation specific humidity and anomalous relative humidity.



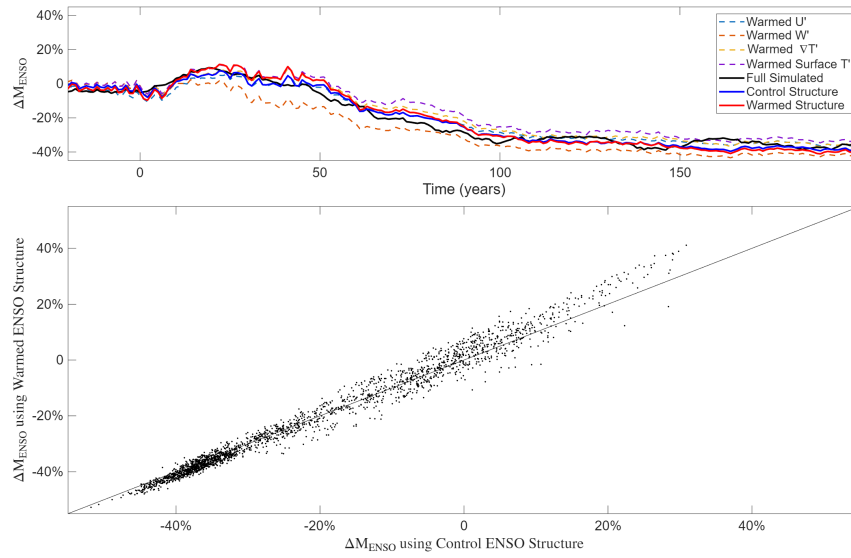
**Extended Data Fig. 4 | The inter-model spread of ENSO's response to warming.** Diagnostics of the intermodel-spread of ENSO's response to warming. The top-left panel shows ENSO strength over time across the CMIP abrupt  $4xCO_2$  ensemble, while the bottom-left shows this time series normalized by the final warming amount. The top-right shows a histogram of  $\alpha$  diagnosed as the peak ENSO strength divided by temperature change at that time, and the bottom-right shows a histogram of  $\alpha + \beta$  diagnosed as the steady state ENSO change divided by the steady state temperature change (last 20 years assumed to be in steady-state). In the right two panels, the fit values from MITgcm and CESM2 are also indicated.



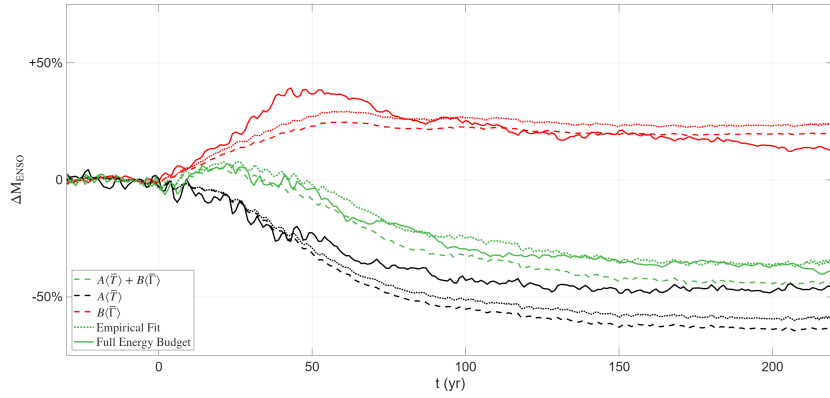
**Extended Data Fig. 5 | Sample temperature trajectories from CESM across SSP scenarios.** Sample temperature trajectories used to predict ENSO, capturing the temperature evolution with a few parameters and how they compare to various scenarios simulated by CESM2.



**Extended Data Fig. 6 | Predicted vs. Simulated ENSO Peaks.** The maximum  $T'$  achieved by simulated El Niño peaks compared to those predicted from the budget discussed and the identity line ( $x = y$ , red) as a basis of comparison. 25 El Niño events from each simulation are shown. For this figure  $\tau_0$  is defined as when  $\langle T' \rangle$  crosses 1 K.



**Extended Data Fig. 7 | The effect of changing ENSO structure on predicted magnitude.** How using the control or warmed ENSO structure alters ENSO magnitude predictions. The top panel shows the same time series as Fig. 3 but using the control or warmed structure or a mixture (i.e., most variables from the reference composite and one variable from the warmed composite), while the bottom panel shows the relationship between the control and warmed ENSO structure predictions.



**Extended Data Fig. 8 | Predicting ENSO Magnitude from calculated and empirically fit parameters.** ENSO magnitude over time, comparing the energy budget approximations given by Eq. 6 (dashed), the linear model (dotted), and the full energy budget (solid). For each of the three, the result of changing stratification (red), mean temperature (black), or the full time evolution (green) are shown.

**Extended Data Table 1 | Empirically fit vs. energy balance predicted models of ENSO variability.** Comparing empirically fit and predicted parameters for the first linear model applied to the MITgcm. The corresponding time series are shown in Extended Data Fig. 8.

Parameter	Empirical fit	Energy budget prediction	Error
A (1/K)	-0.14	-0.15	7%
B (m/K)	7.8	6.6	15%

**Extended Data Table 2 | Fit parameters for each linear model.** Values of the relevant parameters for the two linear models, calculated as discussed in the main text and methods section.

Variable	MITgcm	CESM2-LE	CMIP Ensemble Abrupt
A (1/K)	-0.14		
B (m/K)	7.8		
$\alpha$ (1/K)	0.04	0.21	0.10
$\beta$ (1/K)	-0.07	-0.29	-0.11
$t_{\text{lag}}$ (yr)	34.6	28.2	21.5

# Supplemental Information: The Rise and Fall of ENSO in a Warming World: Insights from a Lag-Linear Model

P.J. Tuckman<sup>1\*</sup> and Da Yang<sup>1,2\*</sup>

<sup>1</sup>Department of Geophysical Sciences, University of Chicago, 5734 S Ellis Ave, Chicago, IL, 60637, United States of America.

<sup>2</sup>Department of Geophysics, Stanford University, 397 Panama Mall, Stanford, CA, 94305, United States of America.

\*Corresponding author(s). E-mail(s): [pjt5@uchicago.edu](mailto:pjt5@uchicago.edu);  
[dayang@stanford.edu](mailto:dayang@stanford.edu);

## **This file includes:**

Supplementary Text 1: Surface Fluxes and Warming .....	Page 2
Supplementary Text 2: Predicting Linear Model Coefficients .....	Page 4
Supplementary Text 3: Connecting the Linear Models .....	Page 6
Supplementary Figures 1 to 4 .....	Page 7

# 1 Surface Fluxes and Warming

Here, the weakening of ENSO events due to strengthened surface flux damping is discussed in detail. This effect is controlled by latent heat fluxes and driven by the increase in saturation specific humidity with warming.

The sum of sub-grid-scale processes (i.e., radiation and turbulent fluxes) is a damping effect in all climates, meaning it is negatively correlated with surface temperatures (Extended Data Fig. 3a). When the mean temperature is larger, i.e., in a warmer climate, the slope of this relationship increases, making surface fluxes a stronger damping effect. Anomalous latent heat flux (LHF', scaled by the heat capacity of the mixed layer so it has units of temperature tendency) shows these same features (Extended Data Fig. 3b) – it is a damping effect and the relevant slope steepens with warming. The strength of total surface flux damping, represented by  $\bar{\alpha}_{\text{SF}}$  in the main text, is shown as a function of time in Extended Data Fig. 3c and, as expected, it becomes more negative with warming. To decompose  $\bar{\alpha}_{\text{SF}}$ , we define an  $\bar{\alpha}$  for each variable such that  $\bar{\alpha}_x$  is the slope of the relationship between  $x'$  and  $\text{SST}'$  for positive values of  $\text{SST}'$  within 10 years on either side of time  $t$ . The LHF and total  $\bar{\alpha}$  values are similar, and the increase with warming of the total  $\bar{\alpha}_{\text{SF}}$  is controlled by that of LHF. Therefore, the strengthening of surface flux damping with warming is associated with LHF, i.e. evaporation from the ocean surface into the boundary layer.

To understand why  $\bar{\alpha}_{\text{LHF}}$  increases with warming, we consider the bulk formula for evaporation in climate models:

$$\text{LHF} = C_d |\bar{u}| q^* (1 - \text{RH}) = C q^* (1 - \text{RH}) \quad (1)$$

where  $C_d$  is a constant coefficient,  $|\bar{u}|$  is the wind speed, and  $q^*(1 - \text{RH})$  is the saturation deficit, or the difference between the saturation specific humidity of the SST and the specific humidity of the lowest atmospheric level. The second expression consolidates the two variables which do not change significantly with warming into a constant  $C$ . We wish to study anomalous fluxes:

$$\text{LHF}' \approx C' \overline{q^* (1 - \text{RH})} + \overline{C q^* (1 - \text{RH})} - \overline{C q^* \text{RH}'} \quad (2)$$

where non-linear terms are ignored. Calculating  $\bar{\alpha}$  values for each anomalous variable, we find:

$$\bar{\alpha}_{\text{LHF}} \approx \bar{\alpha}_C \overline{q^* (1 - \text{RH})} + \overline{C \bar{\alpha}_{q^*} (1 - \text{RH})} - \overline{C q^* \bar{\alpha}_{\text{RH}}}. \quad (3)$$

These three components and their sum are shown in Extended Data Fig. 3d. Their sum is almost identical to  $\bar{\alpha}_{\text{LHF}}$ , indicating that the non-linear terms are indeed small. More importantly, we see that the  $-\overline{C q^* \bar{\alpha}_{\text{RH}}}$  term is causing most of the change in the overall surface flux damping. To understand why this is, we examine the impact of changing  $\bar{q}^*$  or  $\bar{\alpha}_{\text{RH}}$  only, and see that the changes in  $\bar{q}^*$  are causing the overall decrease in  $\bar{\alpha}_{\text{LHF}}$ . In fact, this term alone has a decrease of about 0.6 1/year between the reference and warmed climate, while the total  $\bar{\alpha}_{\text{SF}}$  decreases by 0.65 (panel c). Physically, this change represents that the increase in saturation specific humidity with warming ( $\bar{q}^*$ ) causes a given anomalous relative humidity ( $\text{RH}'$ ) to be associated with a larger saturation deficit ( $q^*(1 - \text{RH})$ ), and therefore more latent heat fluxes,

in a warmer climate. Thus, the increase in saturation specific humidity caused by the Clausius-Clapeyron relationship leads to strengthened surface flux damping in a warmer climate.

## 2 Predicting Linear Model Coefficients from Energy Balance

We here use East Pacific energy balance and the MITgcm  $\Delta t = 50$  year simulations to estimate the coefficients of mean temperature and stratification in the linear model for ENSO amplitude. In other words, we begin with Eq. 3 and derive the expressions in Eq. 6. Our starting point, the energy balance expression for ENSO magnitude, is:

$$\Delta M_{\text{ENSO}}(t) = \exp \left[ \int_{\tau_0}^0 d\tau \left( -\frac{\langle \Delta \bar{\mathbf{u}} \cdot \nabla T' \rangle}{\langle T' \rangle} - \frac{\langle \mathbf{u}'_h \cdot \Delta \nabla_h \bar{T} \rangle}{\langle T' \rangle} - \frac{\langle w' \Delta \bar{\Gamma} \rangle}{\langle T' \rangle} - \Delta \bar{\alpha}_{\text{SF}} \frac{\langle T' \rangle_{2\text{D,surf}}}{\langle T' \rangle} \right) \right] - 1.$$

We Taylor expand the exponential function and keep only the linear term to find

$$\Delta M_{\text{ENSO}}(t) = \int_{\tau_0}^0 d\tau \left( -\frac{\langle \Delta \bar{\mathbf{u}} \cdot \nabla T' \rangle}{\langle T' \rangle} - \frac{\langle \mathbf{u}'_h \cdot \Delta \nabla_h \bar{T} \rangle}{\langle T' \rangle} - \frac{\langle w' \Delta \bar{\Gamma} \rangle}{\langle T' \rangle} - \Delta \bar{\alpha}_{\text{SF}} \frac{\langle T' \rangle_{2\text{D,surf}}}{\langle T' \rangle} \right).$$

Fig. 4a and b showed that each term in this expression is proportional to either changes in mean temperature or stratification. Tbl. 1 shows details of these relationships, specifically the proportionality constants and  $R^2$  values between each term and the relevant mean variable. Given these proportionalities, we can define constants such that:

$$\Delta M_{\text{ENSO}}(t) = (A_{\bar{\mathbf{u}}} + A_{\nabla_h \bar{T}} + A_{\alpha}) \langle \Delta \bar{T} \rangle + B \langle \Delta \bar{\Gamma} \rangle \quad (4)$$

where:

$$\begin{aligned} A_{\bar{\mathbf{u}}} &= \frac{1}{\langle \Delta \bar{T} \rangle} \int_{\tau_0}^0 d\tau \left( \frac{-\langle \Delta \bar{\mathbf{u}} \cdot \nabla T' \rangle}{\langle T' \rangle} \right) \\ A_{\nabla_h \bar{T}} &= \frac{1}{\langle \Delta \bar{T} \rangle} \int_{\tau_0}^0 d\tau \left( \frac{-\langle \mathbf{u}'_h \cdot \Delta \nabla_h \bar{T} \rangle}{\langle T' \rangle} \right) \\ A_{\bar{\alpha}_{\text{SF}}} &= \frac{1}{\langle \Delta \bar{T} \rangle} \int_{\tau_0}^0 d\tau \left( -\Delta \bar{\alpha}_{\text{SF}} \frac{\langle T' \rangle_{2\text{D,surf}}}{\langle T' \rangle} \right) \\ B &= \frac{1}{\langle \Delta \bar{\Gamma} \rangle} \int_{\tau_0}^0 d\tau \left( \frac{-\langle w' \Delta \bar{\Gamma} \rangle}{\langle T' \rangle} \right). \end{aligned} \quad (5)$$

To obtain this equation, we have simply multiplied each term by unity in the form of either  $\langle \Delta \bar{T} \rangle / \langle \Delta \bar{T} \rangle$  or  $\langle \Delta \bar{\Gamma} \rangle / \langle \Delta \bar{\Gamma} \rangle$ .

Intuitively, the  $A$  terms are inverse temperature scales that represent the mean climate warming over which ENSO strength changes by a factor of  $e$  (before Taylor expanding), and  $B$  is similar but for stratification. Summing the  $A$  terms, our final expression is:

$$\Delta M_{\text{ENSO}}(t) = A \langle \Delta \bar{T} \rangle + B \langle \Delta \bar{\Gamma} \rangle \quad (6)$$

**Table 1** Proportionality constants and  $R^2$  values for the energy budget terms and relevant mean quantities.

Independent Variable	Dependent Variable	Proportionality constant	$R^2$
$\langle \Delta \bar{T} \rangle$	$\int_{\tau_0}^0 d\tau \left( \frac{-\langle \Delta \bar{u} \partial T' / \partial x \rangle}{\langle T' \rangle} \right)$	0.13 (1/K)	0.95
	$\int_{\tau_0}^0 d\tau \left( \frac{-\langle \Delta \bar{v} \partial T' / \partial y \rangle}{\langle T' \rangle} \right)$	0.01 (1/K)	0.91
	$\int_{\tau_0}^0 d\tau \left( \frac{-\langle \Delta \bar{w} \partial T' / \partial z \rangle}{\langle T' \rangle} \right)$	-0.21 (1/K)	0.94
	$\int_{\tau_0}^0 d\tau \left( \frac{-\langle u' \Delta \partial \bar{T} / \partial x \rangle}{\langle T' \rangle} \right)$	-0.02 (1/K)	0.59
	$\int_{\tau_0}^0 d\tau \left( \frac{-\langle v' \Delta \partial \bar{T} / \partial y \rangle}{\langle T' \rangle} \right)$	-0.04 (1/K)	0.98
	$\int_{\tau_0}^0 d\tau \left( -\Delta \bar{\alpha}_{\text{SF}} \frac{\langle T' \rangle_{2\text{D},\text{surf}}}{\langle T' \rangle} \right)$	-0.02 (1/K)	0.85
$\langle \Delta \bar{\Gamma} \rangle$	$\int_{\tau_0}^0 d\tau \left( \frac{-\langle w' \Delta \bar{\Gamma} \rangle}{\langle T' \rangle} \right)$	6.59 (m/K)	0.50

where  $A = A_{\bar{u}} + A_{\nabla_h \bar{T}} + A_{\bar{\alpha}_{\text{SF}}}$ .

Grouping the terms proportional to mean temperature, we can predict the linear model coefficients as:

$$\begin{aligned}
 A &= \frac{1}{\langle \Delta \bar{T} \rangle} \left[ \int_{\tau_0}^0 d\tau \left( \frac{-\langle \Delta \bar{\mathbf{u}} \cdot \nabla T' \rangle}{\langle T' \rangle} + \frac{-\langle \mathbf{u}'_h \cdot \Delta \nabla_h \bar{T} \rangle}{\langle T' \rangle} - \Delta \bar{\alpha}_{\text{SF}} \frac{\langle T' \rangle_{2\text{D},\text{surf}}}{\langle T' \rangle} \right) \right] \\
 B &= \frac{1}{\langle \Delta \bar{\Gamma} \rangle} \int_{\tau_0}^0 d\tau \left( \frac{-\langle w' \Delta \bar{\Gamma} \rangle}{\langle T' \rangle} \right).
 \end{aligned} \tag{7}$$

These expressions, calculated as the proportionality constant between the energy balance term and the mean quantity across all  $\Delta t = 50$  year data, give the values shown in Extended Data Table. 1, within 7% and 15% of the empirical best fits. Using these values instead of the empirical fit gives similar predictions for  $\Delta M_{\text{ENSO}}$ , shown in Extended Data Fig. 8. To summarize, we can use energy balance to qualitatively and quantitatively show that changes to ENSO with warming are accurately described by only mean temperature and stratification, enabling a simple linear predictor to capture much of the future of ENSO variability.

### 3 Connecting the Linear Models

In this section, we quantitatively connect the two linear models for ENSO variability:

$$\begin{aligned}\Delta M_{\text{ENSO}} &= A\langle\Delta\bar{T}\rangle + B\langle\Delta\bar{\Gamma}\rangle \\ &= \alpha\langle\Delta\bar{T}\rangle_{\text{global}} + \beta\langle\Delta\bar{T}(t - t_{\text{lag}})\rangle_{\text{global}}\end{aligned}\quad (8)$$

Relating these models requires linear relationships between the changes in relevant variables under warming; we represent these proportionalities with slopes  $m_n$ . Replacing stratification with the difference between East Pacific surface temperature  $\langle\Delta\bar{T}\rangle_{2\text{D},\text{surf}}$  and East Pacific subsurface temperature  $\langle\Delta\bar{T}\rangle_{2\text{D},\text{subsurf}}$ , then assuming East Pacific mixed layer temperature  $\langle\Delta\bar{T}\rangle$  is proportional to East Pacific surface temperature via slope  $m_1$ :

$$\Delta M_{\text{ENSO}} = Am_1\langle\Delta\bar{T}\rangle_{2\text{D},\text{surf}} + \frac{B}{\Delta z} [\langle\Delta\bar{T}\rangle_{2\text{D},\text{surf}} - \langle\Delta\bar{T}\rangle_{2\text{D},\text{subsurf}}]. \quad (9)$$

Next, we replace subsurface temperature with a constant  $m_2$  multiplied by subtropical surface temperatures with a lag, then assume East Pacific and subtropical surface temperatures are both proportional to global mean surface temperature via slopes  $m_3$  and  $m_4$ :

$$\Delta M_{\text{ENSO}} = \left[ Am_1 + \frac{B}{\Delta z} \right] m_3\langle\Delta\bar{T}\rangle_{\text{global}} - \frac{B}{\Delta z} m_2 m_4 \langle\Delta\bar{T}(t - t_{\text{lag}})\rangle_{\text{global}} \quad (10)$$

Comparing these expressions to the lag-linear model:

$$\begin{aligned}\alpha &= \left[ Am_1 + \frac{B}{\Delta z} \right] m_3 \\ \beta &= -\frac{B}{\Delta z} m_2 m_4\end{aligned}\quad (11)$$

Using the lines of best fit displayed in Fig. S.2, we find that  $\alpha = 0.01$  1/K and  $\beta = -0.04$  1/K, which are the same order of magnitude but significantly different from the fitted values displayed in Extended Data Table 2. Most of the error comes from 1. the relationship between East Pacific and global surface temperatures not being exactly linear (likely related to the pattern effect, Fig. S.2a), or 2. the lag between subtropical and subsurface temperatures depending on the timescale of warming (non-linearities in the green line in Fig. S.2a). The particularly large error in  $\alpha$  is due to it being a small residual between two larger terms ( $Am_1$  and  $B/\Delta z$ ); the uncertainties of  $A$  and  $B$  add together to give a large relative uncertainty in  $\alpha$  because its estimated value is small relative to  $Am_1$  or  $B/\Delta z$ . Overall, we can quantitatively connect our two linear models to understand what controls the parameters, but if we wish to accurately predict ENSO, it is better to use an empirical fit.

## Supplemental Figures

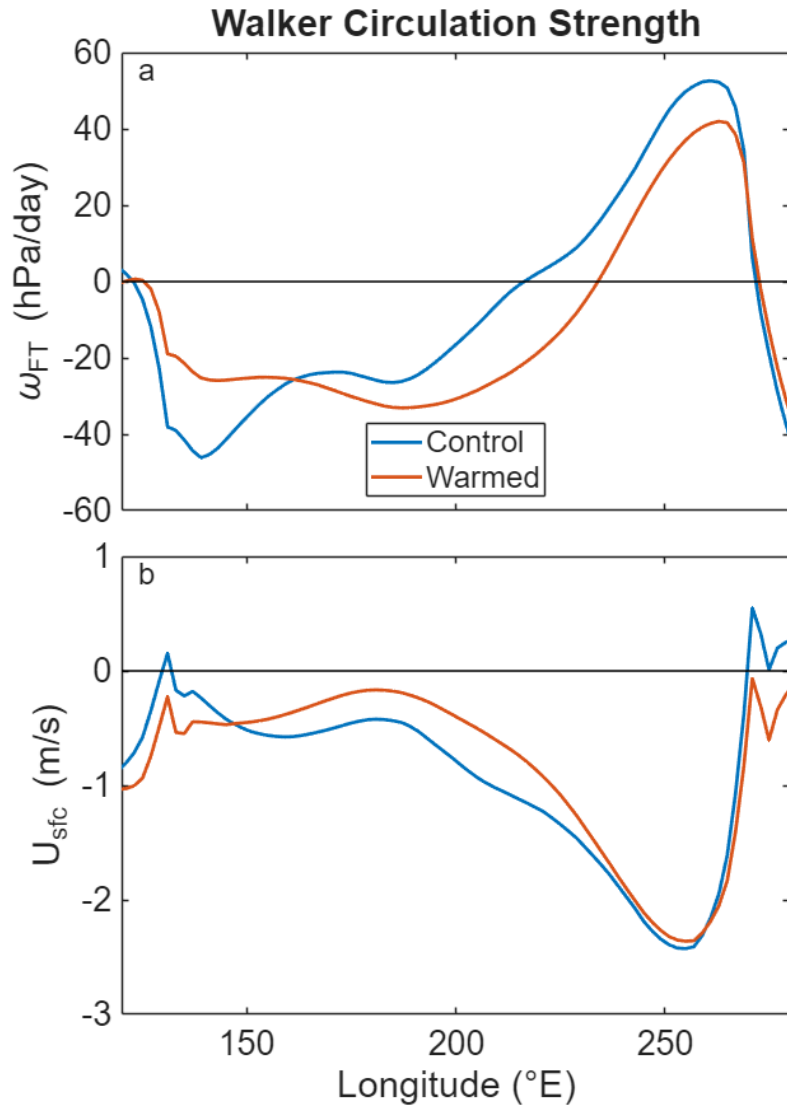


**Fig. S.1** Changes to the Walker circulation with warming. Panel a shows free tropospheric vertical velocity at  $\sim 500$  hPa, while the bottom panel shows zonal velocity at the lowest model level. Wind speeds are averaged within  $5^\circ$  of the equator and compared between the reference simulation (blue) and the  $\Delta t = 10$ yr warming simulations (red). The ascending motion ( $\sim 130$ - $150^\circ$ E), descending motion ( $\sim 260^\circ$ E), and trade winds ( $\sim 160$ - $230^\circ$ E) are all weaker in a warmer climate.

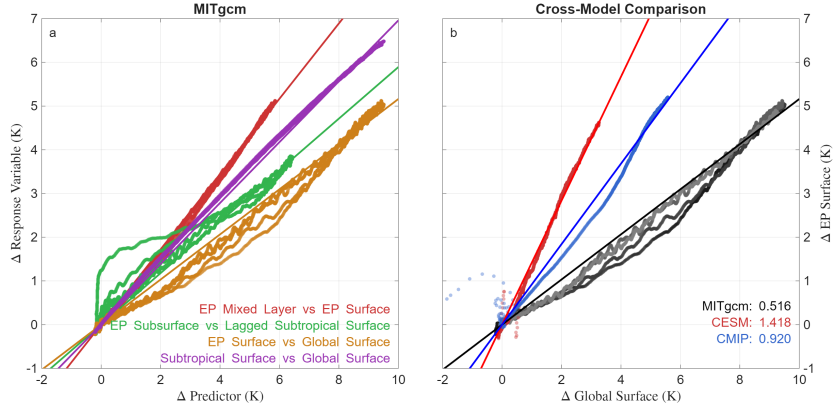


**Fig. S.2** The relevant linear relationships for connecting our two linear models (a) and how one of these relationships is different models (b). Panel b also shows the slopes of the relationships between East Pacific and global mean surface temperatures across each system studied.

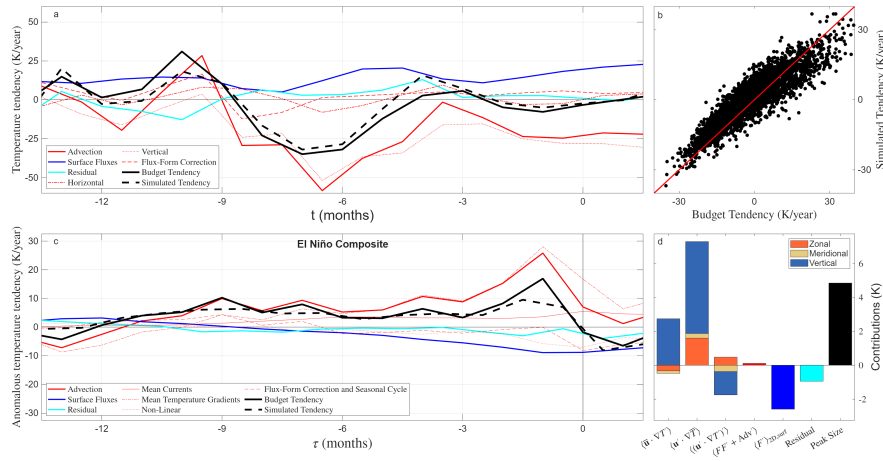


**Fig. S.3** Temperature budget calculations for the East Pacific mixed layer. Panel a shows a sample time series of simulated temperature tendency (dashed black line), its advective (red) and surface flux (blue) contributions, and the resulting predicted budget tendency (sum of right hand side of Eq. 10 solid black). The residual (cyan) and advection sub-components (thin red lines; horizontal, vertical, and seasonal cycle and flux form correction) are also shown. Panel b shows the degree to which the budget tendency matches simulated temperature changes at all times in the control simulation. Panel c shows a similar budget for an El Niño composite as a function of time relative to the peak  $\tau$ . Each quantity is averaged over 25 events from the control simulation, chosen as those with the maximum values of  $\langle T' \rangle$  divided by the moving standard deviation separated by at least two years. Panel d shows the integral of each term up to  $\tau = 0$ , i.e., their contribution to the total El Niño peak.

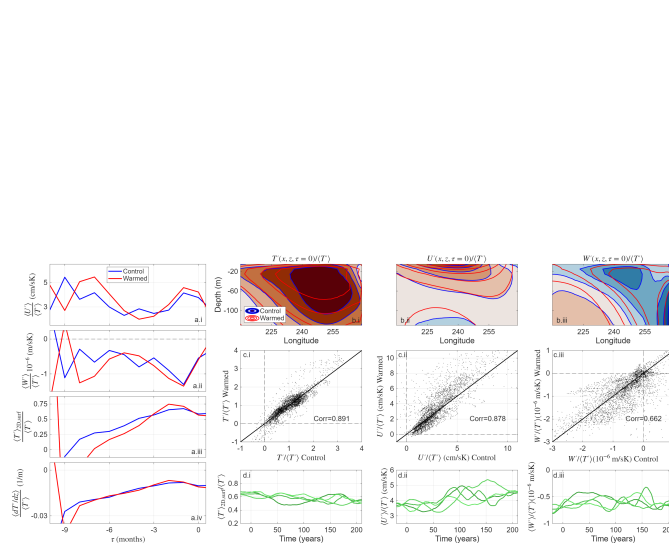


**Fig. S.4** How the structure of ENSO events change under warming. Panel a shows the volume averaged anomalous zonal (a.i) and vertical currents (a.ii), surface temperature (a.iii), and stratification (a.iv) as a function of  $\tau$ , all normalized by the anomalous temperature and shown for the quasi-steady-state control and warmed climates. Panel b shows longitude-depth slices at  $\tau = 0$  of anomalous temperature (b.i), zonal current (b.ii), and vertical current (b.iii), also normalized and displayed for the control and warmed climates. Panel c shows the correlation between the control and warmed normalized anomalies for the same three quantities across all values of  $\tau$ ,  $x$ ,  $y$ , and  $z$  in the relevant region and after  $\tau_0$ . Lastly, panel d shows how relevant anomalous quantities change over time, where the value at each time is calculated from the composite of the 20 ENSO events closest to that point in time across all simulations with the same warming timescale. As with the figures in the main text, the color corresponds to the warming timescale.